

Enantiosensitive locking of photoelectron spin and cation orientation

Philip Caesar M. Flores¹, Stefanos Carlström¹, Serguei Patchkovskii¹, Misha Ivanov^{1,2,7}, Vladimiro Mujica³, Andres F. Ordonez^{1,4,5} and Olga Smirnova^{1,6,7}

¹*Max-Born-Institut, Max-Born-Str. 2A, 12489 Berlin, Germany*

²*Institute of Physics, Humboldt University zu Berlin, Berlin 12489, Germany*

³*School of Molecular Sciences, Arizona State University, Tempe, AZ 85287-1604, USA*

⁴*Department of Physics, Imperial College London, SW7 2BW London, United Kingdom*

⁵*Department of Physics, Freie Universität Berlin, 14195 Berlin, Germany*

⁶*Technische Universität Berlin, Straße des 17. Juni 135, 10623 Berlin, Germany*

⁷*Technion - Israel Institute of Technology, Haifa, Israel*

Chirality describes the asymmetry between an object and its mirror image, underpinning diverse functionalities across all scales of matter—from molecules and aggregates to thin films and bulk chiral materials. A particularly intriguing example is chirality-induced spin selectivity (CISS), where chiral structures orient electron spins enantio-sensitively. Despite extensive research, the fundamental origin of spin–chirality coupling, the unexpectedly large magnitude of the CISS effect, and the possible role of electromagnetic fields remain unclear. Here, we address these issues by examining the simplest scenario: spin-resolved photoionization of randomly oriented chiral molecules. We uncover two universal geometric mechanisms of spin-selective photodynamics, arising solely from electric-dipole interactions and previ-

ously unrecognized. These mechanisms operate effectively even in amorphous chiral media under isotropic illumination and persist at weak spin–orbit coupling, underscoring fundamental aspects of spin–chirality interplay. We further identify an unreported phenomenon central to CISS: locking of photoelectron spin orientation to molecular geometry. Our findings provide a unified geometric framework with broad implications, extending from CISS and asymmetric catalysis to spin textures in chiral crystals and chiral quantum materials such as Weyl semimetals.

Chiral molecular interactions are a remarkable example of a geometrically robust response active in living matter, maintained in complex and noisy environments and operating at ambient conditions ^{1,2}. It has potential for applications, e.g., in quantum technologies ^{3–7}, with chirality-induced spin selectivity (CISS) being an example of useful functionality ⁸. Originally observed as enantio-sensitive electron spin polarization upon transport through chiral biomolecules ^{9,10}, CISS now underscores a broad range of electronic processes where molecular chirality governs spin polarization ^{1,8}. Beyond molecular systems, solid-state materials with chiral crystal lattices exhibit a related but more complex influence on spin: they stabilize noncollinear spin textures such as skyrmion crystals — topologically nontrivial spin configurations whose formation and control are governed by the chirality of the lattice.

Many CISS phenomena are induced by light, suggesting the possibility of ultrafast control over spin-sensitive chemical processes via photoexcitation or photoionization. The interplay between spin and chirality naturally suggests spin-orbit coupling (SOC) as the underlying mechanism

for spin selectivity. However, several experiments have shown that SOC alone cannot explain the observed effect ^{11–13}. Numerous theoretical approaches including scattering theory ^{14–17}, tight-binding models ^{18–22}, density functional theory ^{23–25}, scattering off magnetic impurities ²⁶, electron correlation models ²⁷, and field-theoretical treatments ²⁸ have been proposed, yet a complete understanding remains elusive ¹. Diverse challenges for interpretation emerge due to the presence of multiple factors that potentially affect this process in experimental measurements thereby complicating its analysis, e.g., leads or substrates for molecules, and impurities, defects, or spurious fields for solids. To date, studies of enantio-sensitive spin dynamics have mainly focused on inherently weak effects related to the magnetic-field component of light ²⁹.

Here, we examine the simplest yet ubiquitous example of spin-chirality coupling: spin-resolved photoionization of randomly oriented chiral molecules. Once ambiguities related to anisotropic targets or substrates, and complex detection schemes involving leads are removed, fundamental origins of spin-chirality coupling associated with photodynamics emerge with a striking clarity in an approach which is equally applicable to photoionization and photoexcitation of randomly oriented molecules. We find that molecular chirality couples to intrinsic directional biases associated with electron spin or photon spin, which become observable once these spins are specified in the laboratory frame. We rigorously show that these biases are quantified by two pseudovectors stemming from the geometric properties of photoionization dipoles in spin space and in real space. They reflect the propensity for electrons to have specific spin and orbital angular momentum orientations. These geometric features emerge even in the absence of external orientational bias, i.e. in amorphous chiral media, but can be enhanced by anisotropy. Moreover, we

uncover the previously unreported geometric effect capturing the core of CISS: enantio-sensitive locking of molecular orientation to photoelectron spin. In closed-shell molecules, this directly links the spin of the cation (hole) to its orientation, naturally leading to spin-selective phenomena in orientation-sensitive environments, such as interfaces or orientation-dependent molecular reactions.

We find that one of these two complementary *geometric mechanisms* operates in fields of arbitrary polarization, including fully isotropic polarization, and can yield enantio-sensitive spin-orientation locking of up to 40%, even for spin-depolarized initial states. Importantly, both mechanisms bypass the weak magnetic-field interaction, relying solely on electric-dipole interactions between the light field and the molecule. The developed theoretical framework enables rigorous quantification of several complementary mechanisms of enantio-sensitive spin-orientation locking in photoionization.

1 Geometric nature of spin-chirality coupling

To isolate the tandem action of chirality and spin underlying CISS from extrinsic orientational biases, consider a gedanken experiment: photoionization of randomly oriented chiral molecules using light fields with randomly oriented polarization vectors. If the cation orientation locks to the detected spin direction along a laboratory axis \hat{s}^L , we should observe different amounts of cations correlated to spin-up and spin-down electrons along this axis. For this to occur in randomly oriented ensemble, there must exist a unique molecular axis along which the propensity to generate

photoelectrons with a particular spin projection is maximal. Since the illumination is isotropic, the direction and magnitude of this propensity are intrinsic molecular properties.

Our analysis reveals a pseudovector \vec{S} specifying the molecular-frame axis that maximizes spin polarization, with strength given by $|\vec{S}|$. \vec{S} can be understood as the natural molecular spin-quantization axis—that is, the direction in the molecular frame along which the spin polarization of an excited or photoionized electron is maximized. This implies that photoexcitation or photoionization under isotropic illumination, without any influence from the magnetic component of light, can effectively “magnetize” an excited or photoionized molecule. While any molecule may exhibit this property, its implications are particularly significant for chiral molecules.

The combination of \vec{S} and molecular chirality leads to a striking phenomenon: cations correlated with photo-electrons having positive (negative) spin projection onto the detection axis \hat{s}^L are oriented with \vec{S} parallel (antiparallel) to \hat{s}^L . This phenomenon, unique to chiral media, ensures opposite orientations for cations of opposite handedness linked to the same electron spin, and vice versa (see Fig. 1). In closed-shell molecules, where electron spin directly maps onto (opposite) hole spin, unbiased photoionization creates two oppositely oriented cation sub-ensembles, each with \vec{S} parallel to the hole spin but opposite hole-spin directions (Fig. 1).

Mathematically, \vec{S} is a Bloch pseudovector describing spin orientation in the degenerate two-level system formed by spin-up and spin-down continuum states populated by photoionization. It incorporates both populations and coherences within this system. Under isotropic illumination, the Bloch pseudovector induces longitudinal spin-orientation locking, aligning the averaged orienta-

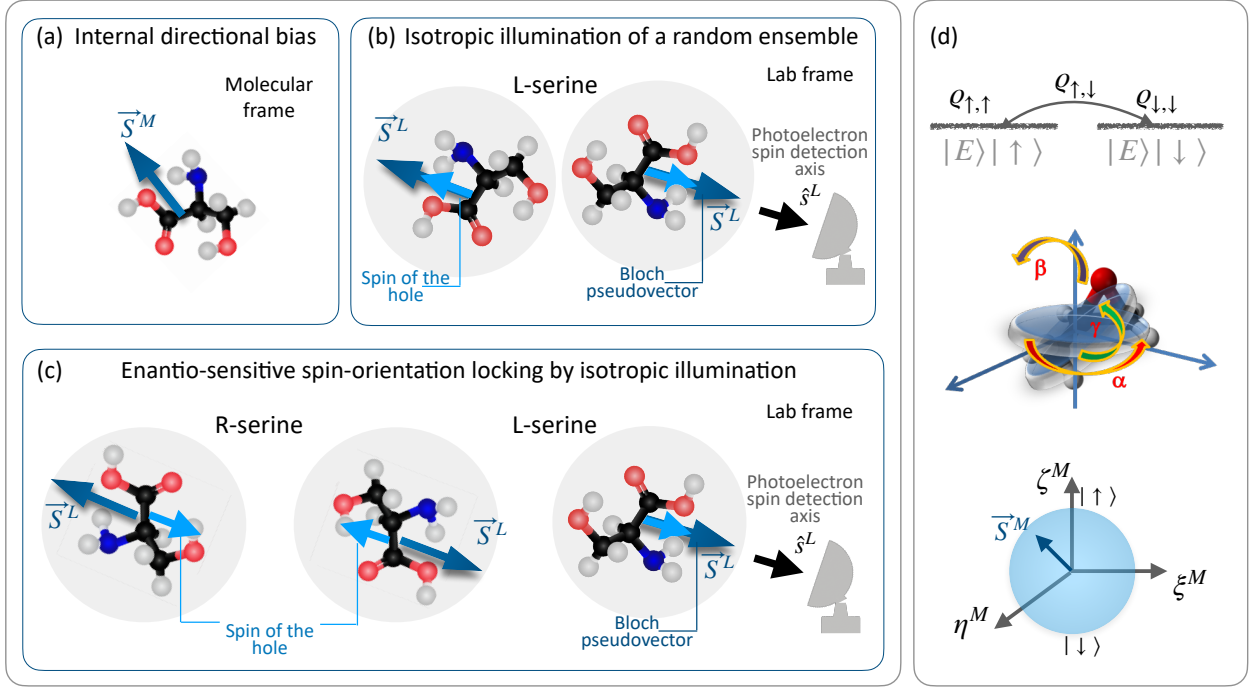


Figure 1: Spin-chirality coupling in photoionization of randomly oriented molecules under isotropic illumination is unique to chiral media. (a) The Bloch vector \vec{S}^M is “attached” to the molecule. (b) After photoionization the cation cloud (gray) possesses a net orientation such that \vec{S}^L is parallel to the spin detection axis \hat{s}^L . Same enantiomers correlated to photoelectrons with opposite spin projections on the axis \hat{s}^L are oriented oppositely. (c) The direction of spin to cation orientation locking is defined by \vec{S}^L such that the photoelectron spin is parallel (antiparallel) to \vec{S}^L for right (left) molecules. (d) Reduced (averaged over molecular orientations) density matrix ρ of a degenerate two-level system corresponding to spin-up $| \uparrow \rangle$ and spin-down $| \downarrow \rangle$ states of the photoelectron with energy $E = \frac{k^2}{2}$. The Bloch vector \vec{S}^M is the expectation value of spin operator for a state with density matrix ϱ . \vec{S}^M is defined on the Bloch sphere in the molecular frame $\{\hat{\xi}^M, \hat{\eta}^M, \hat{\zeta}^M\}$.

tion of cations parallel to the spin detection axis (see Fig. 1). This mechanism is universal in chiral media and is likely also relevant for spin-chirality coupling in photoexcited bound states. However, if $\vec{S} = 0$, then no spin orientation arises under isotropic illumination.

Now, let us relax the isotropic illumination condition and consider fields with polarization planes fixed in the laboratory frame, e.g., circularly or elliptically polarized light. Such fields naturally define an additional spatial axis — the photon spin direction $\hat{\Xi}^L$. Consequently, a new geometric object becomes relevant. It is analogous to the antisymmetric curvature $\vec{\Omega}$ ^{30–33} in spinless systems, where $\vec{\Omega}$ characterizes the propensity for photoionization from states with specific orbital angular momentum projections along the $\hat{\Xi}^L$ axis. Extending this concept to include spin, we find that the spin-dependent curvature emerges as a matrix in spin space.

The spin-dependent curvature defines two fundamental properties of the local, light-induced spin response (a magnetic-like response without magnetic fields): a scalar χ_{gs} and a pseudovector $\vec{\tau}$. Both originate from the spin-resolved curvature matrix but differ by their contraction with the spin operator: χ_{gs} emerges from the trace of their scalar (dot) product, and $\vec{\tau}$ from the trace of their vector (cross) product, highlighting a unified geometric origin.

The *geometric spin susceptibility* χ_{gs} measures how the geometric structure of photoionization dipoles mediates spin orientation induced by photon spin. The spin torque vector $\vec{\tau}$ describes how the same geometry imparts a torque on the photoelectron spin, leading to a counter-intuitive *transversal* enantio-sensitive spin-orientation locking where the cation would be oriented orthogonally to both the electron spin detection axis \hat{s}^L and the photon spin $\hat{\Xi}^L$.

We derive these results below in a fully general and compact approach, and show that for a synthetic chiral system with extremely small ratio ($\simeq 0.01$) of spin-orbit interaction to the ionization potential spin-orientation locking can reach up to 60% for randomly oriented and up to 73% for partially aligned ensembles.

2 Synthetic chiral matter

To quantify spin-chirality coupling in photoionization, we construct spin-resolved chiral electronic states in Ar atoms, rigorously incorporating electronic chirality and spin-orbit coupling. Inspired by analogous chiral hydrogenic states ³⁴, these states combine excited-state orbitals:

$$|\psi_{m,\mu}^{\pm}\rangle = \frac{1}{\sqrt{2}} (|4p_m, \mu\rangle \pm |4d_m, \mu\rangle). \quad (1)$$

To generalize Eq. (1) for a multielectron system such as argon (see Methods), we employ an optimization approach detailed in Appendix A. Unlike hydrogen, the multielectron core potential in argon breaks inversion symmetry, lowering the symmetry of the resulting states (Fig.2). Consequently, synthetic chirality in argon is stabilized by electron correlations making this system ideal for exploring spin-chirality coupling computationally within a fully consistent approach.

3 Geometric spin concepts in the electric dipole regime

The first geometric object, the photoionization Bloch vector, characterizes the interplay between molecular geometry and electron spin, and is independent of the photon spin. Let us introduce a reduced density matrix $\tilde{\varrho}^M$ of a two-level system associated with photoelectron with a given energy

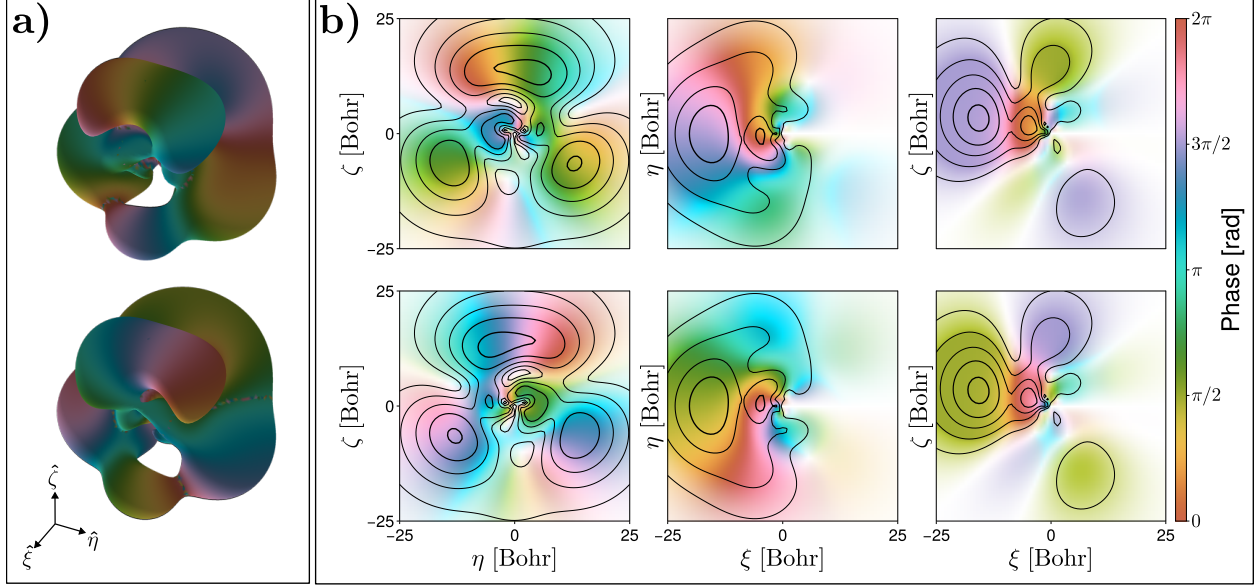


Figure 2: Comparison of the (a) isosurface and (b) contour plots of the chiral electronic states $|\psi_{-1,\frac{1}{2}}^+\rangle$ and $|\psi_{-1,\frac{1}{2}}^-\rangle$ shown in the top and bottom row (in the molecular frame), respectively, and colored according to its phase. The molecular $\{x, y, z\}$ axes are labeled as $\{\xi, \eta, \zeta\}$, respectively. The isosurface is set at $|\psi_{-1,\frac{1}{2}}^\pm| = 3.2 \times 10^{-3}$. The contour plots are cuts on the $\xi = 0$, $\zeta = 0$, and $\eta = 0$ planes. Thicker contour lines and darker shading correspond to higher values of the density. It can be seen that the states $|\psi_{-1,\frac{1}{2}}^\pm\rangle$ are mirror images of each other with a π phase shift, and the probability current rotates in opposite directions.

naturally arising in one-photon ionization:

$$\tilde{\varrho}_{\mu_1, \mu_2}^M = \sum_I \int d\Theta_k^M \left(\vec{D}_{I, \vec{k}^M, \mu_1}^{M*} \cdot \vec{D}_{I, \vec{k}^M, \mu_2}^M \right). \quad (2)$$

Here, $\vec{D}_{I, \vec{k}^M, \mu_1}^M$ is the molecular-frame transition dipole (see Eq. (14) in Methods), the superscript M denotes the molecular frame, $|I\rangle$ labels the final state of the ion, $\mu = \pm \frac{1}{2}$ labels spin projections onto the molecular z-axis¹. $\hat{\zeta}, \vec{k}^M$ is the final photoelectron momentum in the molecular frame, and

¹Our results are invariant with respect to the choice of spin quantization axis in the molecular frame.

$\int d\Theta_k^M$ denotes averaging over all directions of \vec{k}^M . The reduced density matrix Eq.(2) emerges after averaging over random molecular orientations (see Methods).

The geometric nature of Eq.(2) is revealed by expressing it as:

$$\tilde{\varrho}^M = \frac{1}{2} \left(S_0 \mathbb{I} + \vec{S}^M \cdot \hat{\Sigma}^M \right), \quad (3)$$

where $\hat{\Sigma} = \hat{\sigma}^T$, $\hat{\sigma}$ is the vector of the Pauli spin matrices, S_0 is the total ionization rate, and \vec{S}^M is the Bloch vector controlling enantio-sensitive spin-orientation locking,

$$\vec{S}^M = \text{Tr} \left(\tilde{\varrho}^M \hat{\Sigma}^M \right). \quad (4)$$

Both $\tilde{\varrho}^M$ and \vec{S}^M only depend on the photoionization (or photoexcitation) dipoles and encode properties of molecular states.

The second geometric object is sensitive to the photon spin. One can show (see Methods) that the geometry-spin interplay in photoionization induced by the photon spin is described by the matrix Ω , which represents an effective spin-dependent geometric field. Its elements are the curvature pseudovectors $(\Omega)_{\mu_1, \mu_2} \equiv \vec{\Omega}^{(\mu_1, \mu_2)}$:

$$\vec{\Omega}^{(\mu_1, \mu_2)} = \sum_I \int d\Theta_k^M \left(\vec{D}_{I, \vec{k}^M, \mu_1}^{M*} \times \vec{D}_{I, \vec{k}^M, \mu_2}^M \right). \quad (5)$$

This spin-dependent geometric field mediates both non-enantio-sensitive spin orientation via the scalar $\chi_{\text{gs}} \propto \text{Tr} \left(\hat{\Sigma}^M \cdot \Omega^M \right)$ and enantio-sensitive spin-orientation locking via the spin torque pseudovector $\vec{\tau}^M \propto \text{Tr} \left(\hat{\Sigma}^M \times \Omega^M \right)$ (see Methods).

4 Spin-orientation locking in randomly oriented chiral molecules

Spin-orientation locking is a link between the cation orientation characterized by an orientation-averaged value $\langle \vec{V}^L \rangle$ of a molecular vector \vec{V}^L and the electron spin orientation measured along the laboratory \hat{s}^L axis upon one-photon ionization of randomly oriented chiral molecules. Below, we formalise and quantify two main enantio-sensitive mechanisms controlling this link, associated either with the Bloch vector $\langle \vec{V}^L(\hat{s}^L) \rangle_S$ or with the curvature $\langle \vec{V}^L(\hat{s}^L) \rangle_\Omega$:

$$\langle \vec{V}^L(\hat{s}^L) \rangle \equiv \int d\Theta_k^M \int d\rho W^M(\hat{k}^M, \hat{s}^L, \rho) \vec{V}^L = \langle \vec{V}^L(\hat{s}^L) \rangle_S + \langle \vec{V}^L(\hat{s}^L) \rangle_\Omega. \quad (6)$$

Here, $W^M(\hat{k}^M, \hat{s}^L, \rho)$ is the momentum and spin resolved ionization rate for a given molecular orientation ρ (see Methods).

Let us first consider fields that are isotropically polarised in space in order to exclude the effects of molecular frame alignment introduced by the light field upon photon absorption. In this case $\langle \vec{V}^L(\hat{s}^L) \rangle_\Omega = 0$, and $\langle \vec{V}^L(\hat{s}^L) \rangle$ will be driven solely by the photo-ionization Bloch pseudovector \vec{S}^M , yielding (see Appendix D)

$$\langle \vec{V}^L(\hat{s}^L) \rangle^{\text{iso}} = \frac{1}{3S_0} (\vec{V}^M \cdot \vec{S}^M) \hat{s}^L. \quad (7)$$

This mechanism of spin-orientation locking is enantio-sensitive because $\vec{V}^M \cdot \vec{S}^M$ is a molecular pseudoscalar, which changes sign upon inversion. Thus, it vanishes for achiral systems.

Fig.3 shows the degree of spin-orientation locking for different chiral states in our synthetic chiral system, argon, under random illumination as a function of the photoelectron final momentum

$k = \sqrt{2E}$. The black curve in Fig.3 (b) shows results for photoionization from initially spin-depolarised states, corresponding to incoherent superposition of the chiral states with $m = 1$ and $m_s = \pm 1/2$. We see strong spin-orientation locking even in such a small chiral system, with $\langle \hat{e} \cdot \hat{s} \rangle = \langle \cos \beta \rangle \simeq 0.1$ corresponding to about 60% systems oriented in the upper hemisphere relative to 40% in the lower. The Bloch vectors for $m = 1, m_s = \pm 1/2$ are almost orthogonal to each other (see orange and violet arrows in Fig.3 (a)). The Bloch vector in the state $m = +1, m_s = 1/2$ is orthogonal to the chosen spin quantization axis ζ , signifying strong contribution of coherences to the longitudinal spin-orientation locking arising during photoionization. The role of coherences in longitudinal spin polarization has not been identified before, because the latter is usually identified as the z-component of the spin expectation value in the final state, which only reflects the difference in populations of the spin-up and spin-down final states at the detector. Fig.3 also demonstrates that the tip of the Bloch vector traces a trajectory in space as a function of the photoelectron momentum. It further highlights the role of coherences in longitudinal spin-orientation locking: their contribution can strongly vary as a function of the final photoelectron momentum, reflecting different spin-aligning effect of the molecular frame on the photoelectron.

We now turn our attention to the second geometric mechanism of spin-orientation locking associated with spin-resolved curvature operator Ω^M (see Appendix D):

$$\langle \vec{V}^L(\hat{s}^L) \rangle_{\Omega}^{\text{circ}} = \frac{1}{2S_0} \left(\text{Tr}(\Omega^M) \cdot \vec{V}^M \right) \hat{\Xi}^L + \frac{1}{2S_0} \left\{ \left[\text{Tr} \left(\hat{\Sigma}^M \times \Omega^M \right) \right] \cdot \vec{V}^M \right\} \left(\hat{s}^L \times \hat{\Xi}^L \right) \quad (8)$$

Equation (8) contains two objects derived from Ω^M : (i) spin-symmetric curvature pseudovector $\text{Tr}(\hat{\Omega}^M) \equiv \vec{\Omega}_{\frac{1}{2}, \frac{1}{2}}^M + \vec{\Omega}_{-\frac{1}{2}, -\frac{1}{2}}^M$, and (ii) spin curvature torque pseudovector $\vec{\tau}^M \equiv \text{Tr} \left(\hat{\Sigma}^M \times \Omega^M \right)$. Since $\langle \vec{V}^L(\hat{s}^L) \rangle_{\Omega}^{\text{circ}}$ depends on the direction of the photon spin $\hat{\Xi}^L$, it can only be triggered by

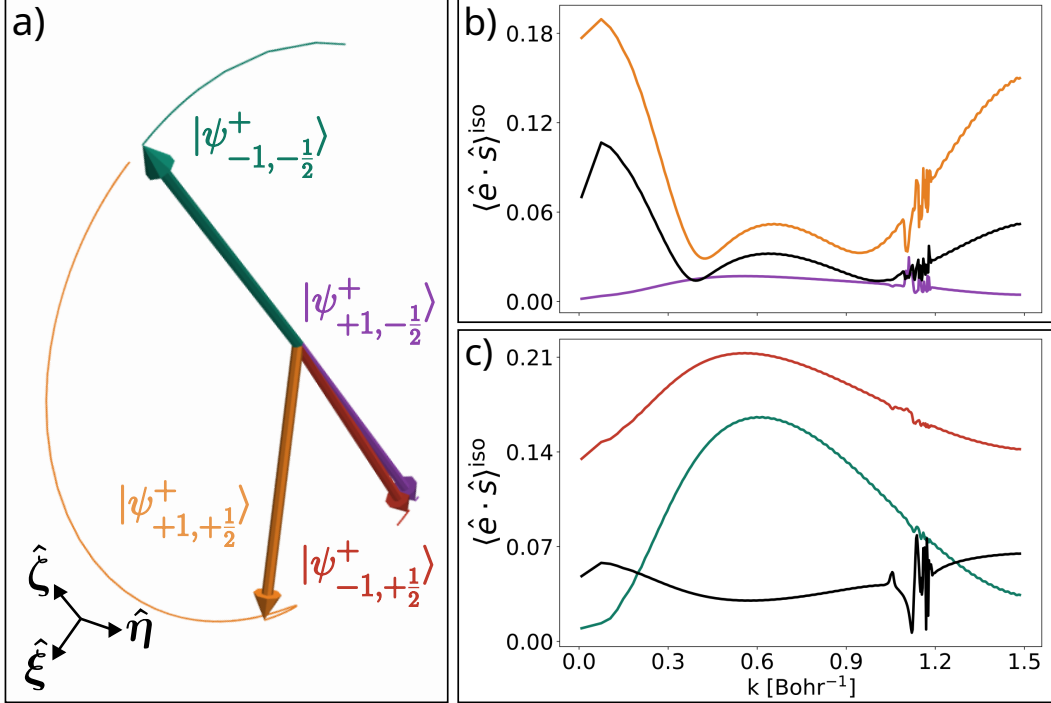


Figure 3: Enantio-sensitive spin-orientation locking under isotropic illumination of randomly oriented electronic states. (a) The Bloch pseudovector \vec{S}^M (internal directional bias) in the molecular frame for the chiral argon states. \vec{S}^M changes its direction in space vs the final momentum of the electron k . Trajectories traced by this vector are shown for $0 < k < 0.8 \text{ Bohr}^{-1}$. (b) Degree of orientation for chiral states with $m = 1, \mu = \pm \frac{1}{2}$ (violet and orange correspondingly), and averaged over spin orientation in initial state (black). (c) Degree of orientation for chiral states with $m = -1, \mu = \pm \frac{1}{2}$ (red and green correspondingly) and averaged (black).

circularly or elliptically polarized light. This mechanism is also enantio-sensitive, since both $(\text{Tr}(\Omega^M) \cdot \vec{V}^M)$ and $\vec{\tau}^M \cdot \vec{V}^M$ are pseudoscalars. Moreover, Eq. (8) shows that $\langle \vec{V}^L(\hat{s}^L) \rangle_\Omega^{\text{circ}}$ lies in the plane spanned by two perpendicular directions: $\hat{\Xi}^L$ and $\hat{s}^L \times \hat{\Xi}^L$. If the photoelectron spin is measured along $\hat{\Xi}^L$, then $\vec{\tau}^M$ is hidden and we see that $\text{Tr}(\hat{\Omega}^M)$ effectively plays a role

analogous to the molecular orientation circular dichroism, MOCD (see Eq. (17) of Ref. ³¹). This term is associated with preferential ionization of those molecules, for which the spin-independent curvature pseudovector $\text{Tr}(\hat{\Omega}^M)$ is oriented along the photon spin direction $\hat{\Xi}$. Since this has been considered elsewhere ³¹, here, we only consider the spin-resolved enantio-sensitive orientation.

The role of the spin curvature torque pseudovector $\vec{\tau}^M$ is revealed by choosing $\hat{s}^L \perp \hat{\Xi}^L$. Specifically, for time-even states (such as the ground state of closed shell molecules) where $\text{Tr}(\Omega^M) = 0$ (see Appendix B), the second term in Eq. (8) features transverse spin-orientation locking: the preferred orientation of the cation is orthogonal to the photoelectron spin detection axis \hat{s}^L . The molecular cation orients in such a way, that the unit vector along the spin curvature torque $\hat{e}_\tau^L \equiv R_\rho [\vec{\tau}^M] / |\tau|$ is parallel to the laboratory axis $\hat{s}^L \times \hat{\Xi}^L$. Therefore, the direction of orientation is controlled by the spin curvature torque pseudovector resulting in spin-locked MOCD (SL-MOCD).

The mechanism based on the photo-ionization Bloch pseudovector also contributes to spin-orientation locking for circularly polarized field, and linearly polarized field with polarization vector $\hat{\epsilon}^L$ (see Appendix D):

$$\langle \vec{V}^L(\hat{s}^L) \rangle_S^{\text{circ}} = \frac{9}{10} \langle \vec{V}^L(\hat{s}^L) \rangle_S^{\text{iso}} + \frac{1}{10S_0} (\vec{S}'^M \cdot \vec{V}^M) \hat{s}^L + \frac{1}{10S_0} [(\vec{S}^M - 3\vec{S}'^M) \cdot \vec{V}^M] (\hat{s}^L \cdot \hat{\Xi}^L) \hat{\Xi}^L, \quad (9)$$

$$\langle \vec{V}^L(\hat{s}^L) \rangle_S^{\text{lin}} = \frac{2}{15} \langle \vec{V}^L(\hat{s}^L) \rangle_S^{\text{iso}} - \frac{1}{5S_0} (\vec{S}'^M \cdot \vec{V}^M) \hat{s}^L + \frac{1}{5S_0} [(3\vec{S}'^M - \vec{S}^M) \cdot \vec{V}^M] (\hat{s}^L \cdot \hat{\epsilon}^L) \hat{\epsilon}^L. \quad (10)$$

Note that $\langle \vec{V}^L(\hat{s}^L) \rangle_S^{\text{circ}}$ is not sensitive to the direction of photon spin since $(\hat{s}^L \cdot \hat{\Xi}^L) \hat{\Xi}^L =$

$(\hat{s}^L \cdot (-\hat{\Xi}^L))(-\hat{\Xi}^L)$. Both phenomena have the same nature, which clearly follows from structurally similar sequence of terms in Eqs. (9) and (10). The first term is the isotropic contribution (Eq. (7)). The next two terms are the consequences of the well-defined direction of light polarization (circular or linear). The partial alignment of the molecular ensemble due to photon absorption is quantified by the additional vector

$$\vec{S}'^M = \text{Re} \sum_{I, \mu_1^M, \mu_2^M} \int d\Theta_k^M \left(\vec{D}_{I, \vec{k}^M, \mu_1^M}^{M*} \cdot \hat{\sigma}_{\mu_1^M, \mu_2^M}^M \right) \vec{D}_{I, \vec{k}^M, \mu_2^M}^M \quad (11)$$

appearing in the second term of Eqs. (9) and (10). The last term is the deviation from the purely longitudinal spin-orientation locking due to the preferential direction introduced by the light field polarization vector $\hat{\epsilon}^L$ or photon spin $\hat{\Xi}^L$.

As anticipated, an additional directional bias introduced by the laser field may enhance the enantio-sensitive spin-orientation locking. For example, in a linearly polarised field and for orthogonal detection geometry ($\hat{s}^L \perp \hat{\epsilon}^L$) enantio-sensitive spin orientation locking reaches extremely high values up to 73% ($\langle \hat{e} \cdot \hat{e} \rangle = 0.3$), see Fig. 4(a), exceeding those for isotropic illumination, see Fig. 4(c). It indicates that partial alignment by photon absorption (the second term in Eq. (10)) indeed enhances the effect. As it is clear from the comparison with the isotropic case (Eq.(7)), in parallel detection geometry ($\hat{s}^L \parallel \hat{\epsilon}^L$) the \vec{S}' in the last term cancels out the second term, moreover the contribution of Bloch pseudovector from the last term in Eq. (10) reduces the isotropic contribution resulting in an overall low signal, Figure 4(b).

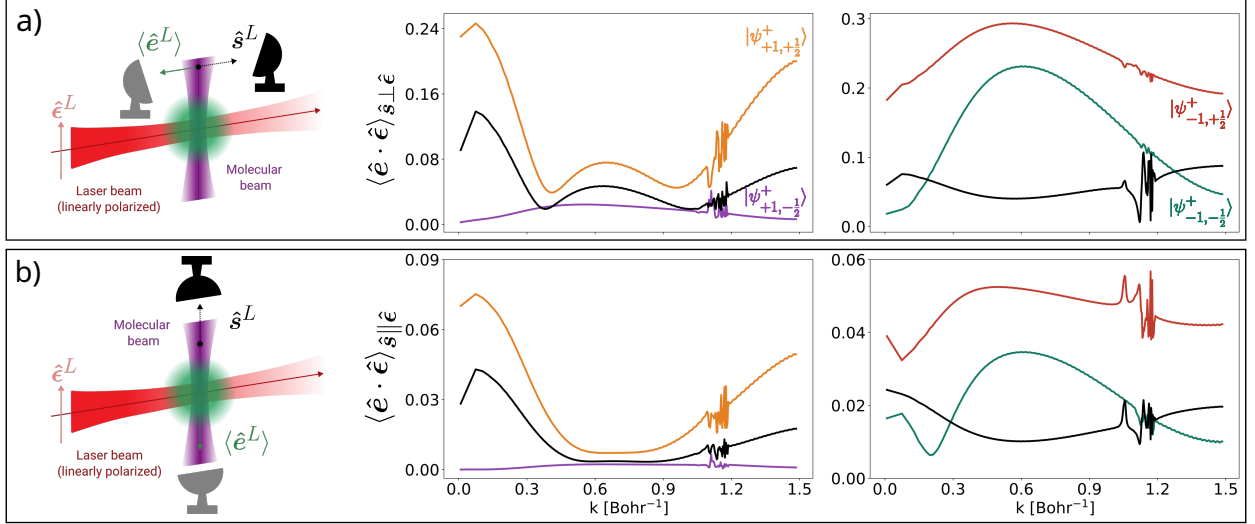


Figure 4: Enantio-sensitive spin-orientation locking resulting from illumination of randomly oriented electronic states by linearly polarised fields (Eq. (10)) in (a) orthogonal detection geometry $\hat{s}^L \perp \hat{\epsilon}^L$ and (b) collinear detection geometry $\hat{s}^L \parallel \hat{\epsilon}^L$. For both panels, $m = 1, \mu = \pm \frac{1}{2}$ (violet and yellow correspondingly) and averaged over spin orientation in initial state (black), while $m = -1, \mu = \pm \frac{1}{2}$ (red and green correspondingly) and averaged black.

5 Interplay between the spin torque and the Bloch mechanisms

Consider photoionization by circularly polarised light, with spin detection axis in the plane of polarization, $\hat{s}^L \perp \hat{\Xi}$. In this case, both mechanisms contribute to enantio-sensitive spin-orientation locking in orthogonal directions. Using Eqs. (6),(8) and (9), we obtain:

$$\langle \hat{e}^L \cdot (\hat{s}^L \times \hat{\Xi}^L) \rangle = \frac{\varsigma}{2S_0} (\hat{e}^M \cdot \vec{\tau}^M), \quad (12a)$$

$$\langle \hat{e}^L \cdot \hat{s}^L \rangle = \frac{3}{10S_0} \left[\hat{e}^M \cdot \left(\vec{S}^M + \frac{1}{3} \vec{S}'^M \right) \right]. \quad (12b)$$

If $\vec{\tau} \perp \vec{S}$, then the two mechanisms could be detected independently. In this case, part of the cations will be oriented such that their spin torque is $\vec{\tau}^L \parallel (\hat{s}^L \times \hat{\Xi}^L)$ and the other part will be oriented such that $(\vec{S}^M + \frac{1}{3}\vec{S}'^M) \parallel \hat{s}^L$. Thus, the ratio of the molecular fragments detected in \hat{s}^L and $(\hat{s}^L \times \hat{\Xi}^L)$ directions quantifies the relative magnitude of the spin torque and Bloch vectors.

If $\vec{\tau} \cdot \vec{S} \neq 0$, then the resulting expectation value of the molecular orientation depends on the angle between the spin torque and Bloch vectors. The cation is then oriented such that its vector $\vec{R}^L \parallel \hat{r}^L$, where

$$\langle \hat{e}^L \rangle = \varsigma(\hat{e}^M \cdot \vec{R}^M) \hat{r}^L, \quad (13a)$$

$$\vec{R}^M = \frac{1}{2S_0} \left[\vec{\tau}^M \cos \alpha + \frac{3}{5} (\vec{S}^M + \frac{1}{3}\vec{S}'^M) \sin \alpha \right], \quad (13b)$$

$$\hat{r}^L = (\hat{s}^L \times \hat{\Xi}^L) \cos \alpha + \varsigma \hat{s}^L \sin \alpha, \quad (13c)$$

$$\alpha = \begin{cases} \alpha_o & , \quad \frac{5}{3} |\vec{\tau}^M|^2 > \frac{3}{5} \left| \vec{S}^M + \frac{1}{3} \vec{S}'^M \right|^2 \\ \alpha_o + \frac{\pi}{2} & , \quad \frac{5}{3} |\vec{\tau}^M|^2 \leq \frac{3}{5} \left| \vec{S}^M + \frac{1}{3} \vec{S}'^M \right|^2 \end{cases} \quad (13d)$$

$$\alpha_0 = \frac{1}{2} \arctan \left[\frac{2\vec{\tau}^M \cdot (\vec{S}^M + \frac{1}{3}\vec{S}'^M)}{\frac{5}{3} |\vec{\tau}^M|^2 - \frac{3}{5} \left| \vec{S}^M + \frac{1}{3} \vec{S}'^M \right|^2} \right]. \quad (13e)$$

The angular distribution of molecular fragments correlated to the spin detected along \hat{s}^L axis maximizes along \hat{r}^L , and the angle between the spin torque and Bloch pseudovectors is encoded in the mixing angle α which can be detected.

Figure 5 quantifies the enantio-sensitive orientation induced by circularly polarised fields ($\varsigma = +1$). In collinear detection geometry $\hat{s}^L \parallel \hat{\Xi}^L$, Figure 5(c) and (d) (right axis, dashed), spin-

orientation locking is driven by the Bloch pseudovector. Comparison of spin-orientation locking for different chiral electronic states reveals its sensitivity to orbital and spin polarization in the initial state. The strongest orientation is achieved for chiral states with initial spin and orbital momentum polarization (Figure 5c). Remarkably, in this case spin-orientation locking up to 60% ($\langle \hat{e} \cdot \hat{\Xi} \rangle = 0.21$, $k = 0.15 \text{ Bohr}^{-1}$) is achieved for counter-rotating electron with spin-up in the initial state ($|\psi_{m,\mu}^+\rangle$), see Figure 5(c). Equally surprising is 40% ($\langle \hat{e} \cdot \hat{\Xi} \rangle = 0.12$, $k = 0.15 \text{ Bohr}^{-1}$) orientation achieved for photoionization of co-rotating electron with depolarized spin $|\psi_{+1}^+\rangle$, see Figure 5(d). Dashed curve in Figure 5(b) quantifies orientation for state with fully depolarised orbital momentum and spin, which still yields significant orientation ($\langle \hat{e} \cdot \hat{r} \rangle = 0.09$, $k = 0.15 \text{ Bohr}^{-1}$).

In the orthogonal detection geometry ($\hat{s}^L \perp \hat{\Xi}^L$) both the spin-torque and the Bloch mechanisms contribute to the final result, orienting the cation in orthogonal directions (see Eqs.(12)). If the mixing angle α is non-zero, this competition results in the final orientation (Eqs.(13)) which encodes the relative angle between the spin torque and Bloch pseudovectors (Eq.(13d)). Figure 5 (left axis, solid) shows that the magnitude of the effect is very similar to the one in collinear detection geometry. However, the orientation occurs in a different direction, that of the vector \hat{r}^L Eq.((13c)). Thus, in our system the Bloch vector mechanism dominates, however, the presence of the spin torque mechanism reveals itself in the direction of orientation. If the spin torque mechanism were not present, the cations would be oriented along \hat{s}^L , not along \hat{r}^L axis rotated away from \hat{s}^L in the plane $\hat{s}^L \times \hat{\Xi}^L - \hat{s}^L$ by the angle α .

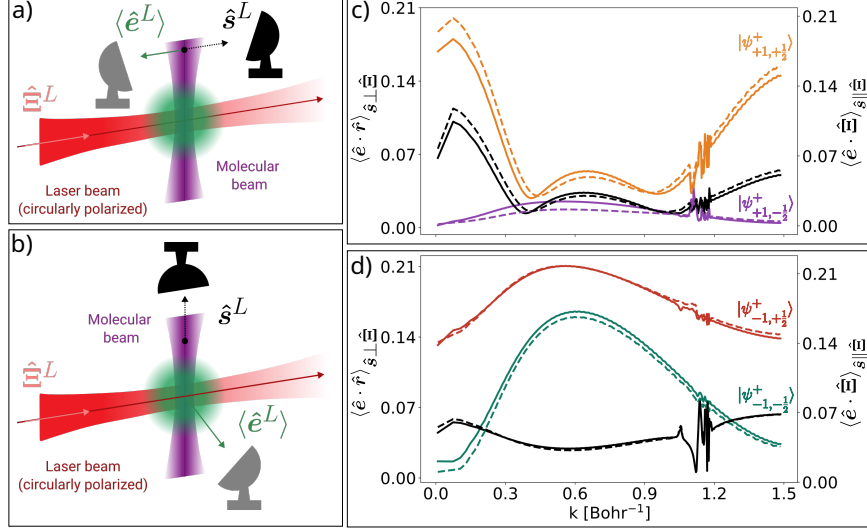


Figure 5: Enantio-sensitive spin-orientation locking resulting from illumination of randomly oriented electronic states by circularly polarised fields for (a) collinear and (b) orthogonal detection geometry. Collinear detection geometry $\hat{s}^L \parallel \hat{\Xi}^L$ corresponding to orientation along $\hat{\Xi}^L$ (dashed lines) is sensitive to the Bloch pseudovector, Eq. (9), while orthogonal detection geometry $\hat{s}^L \perp \hat{\Xi}^L$ corresponding to orientation along \hat{r}^L (solid lines) senses both spin torque and Bloch pseudovectors, Eq. (13). (c) Spin-orientation locking for $m = 1, \mu = \pm\frac{1}{2}$ (violet and orange correspondingly) and averaged over initial spin orientation (black), in detection geometry (a) (dashed, right axis) and geometry (b) (solid, left axis); (d) Same for $m = -1, \mu = \pm\frac{1}{2}$ (red and green correspondingly) and averaged over initial spin orientation (black).

Figure 6 shows the “trajectories” traced by the tips of the vectors $\vec{\tau}^M, \vec{S}^M + \frac{1}{3}\vec{S}'^M \vec{R}^M$ in the molecular frame as a function of the final momentum $k \equiv \sqrt{2E}$ of the photoelectron, for different chiral states. Surprisingly, both $\vec{\tau}^M$ and $\vec{S}^M + \frac{1}{3}\vec{S}'^M$ significantly change their direction in space in the case of photoionization from the chiral state $|\psi_{+1,\pm\frac{1}{2}}^+\rangle$ (orange vector in Fig. 6 a,b,c). Since

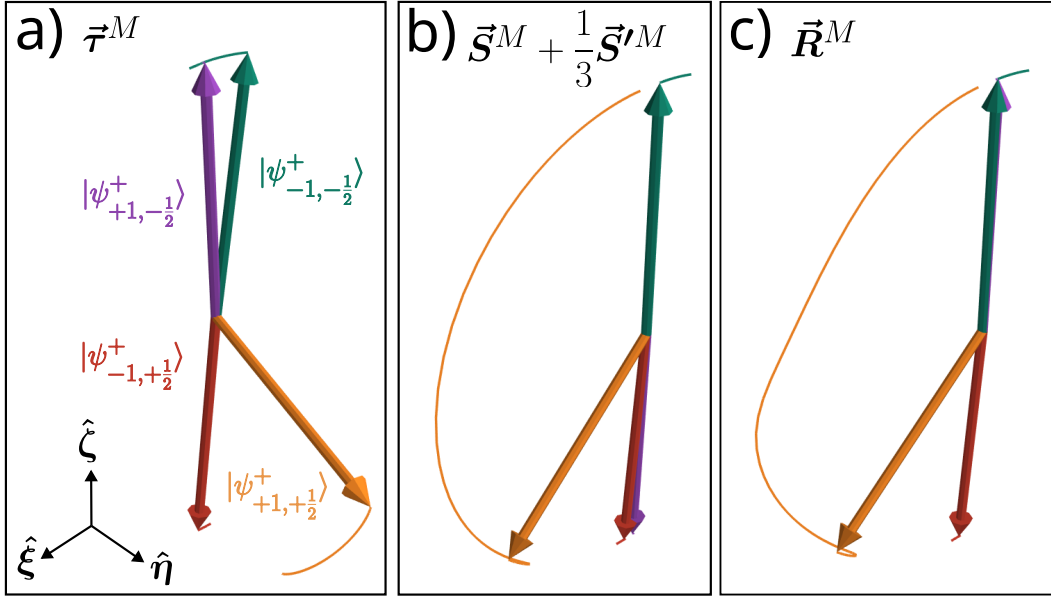


Figure 6: Internal orientation biases described by spin curvature torque vector $\vec{\tau}^M$ (a), the effective Bloch vector $\vec{S}^M + \frac{1}{3}\vec{S}'^M$ (b) and their combination \vec{R}^M (c). The tip of each vector traces a trajectory signifying the rotation of this vector in space, in the molecular frame, as a function of the final momentum $0.15 < k < 0.8 \text{ Bohr}^{-1}$ of the photoelectron.

$\vec{S}^M + \frac{1}{3}\vec{S}'^M$ dominates (see Figure 5), \vec{R}^M follows it closely. Comparing the direction of \vec{S}^M vs k for isotropic illumination (Fig. 3, a) with $\vec{S}^M + \frac{1}{3}\vec{S}'^M$ (Fig. 5,b) one can see that the vector \vec{S}'^M does not contribute strongly. Importantly, the Bloch pseudovector (see orange vector in Fig. 6 b,c) is not oriented along the initially chosen molecular spin-quantization axis ζ , once again highlighting the importance of coherences in enantio-sensitive spin-orientation locking.

Conclusions and Outlook. Spin-chirality coupling in the electric dipole regime in amorphous chiral media can be rigorously quantified via two intrinsic molecular pseudovectors. The first is the spin curvature torque pseudovector $\vec{\tau}$ generated by the spin-resolved curvature operator

Ω . The second is the photoionization Bloch pseudo-vector \vec{S} . These are molecular frame properties, derived from spin-resolved photoionization dipoles. The first manifests in photo-ionization in circularly or elliptically polarized fields and leads to transverse locking of the molecular orientation to the photoelectron spin. The second manifests in fields of arbitrary polarization, even for isotropic polarization directions, and leads predominantly to longitudinal spin-orientation locking. While these basic mechanisms present elementary blocks of spin-chirality coupling, we expect that they will be complemented by additional effects associated with specific geometries or orientational anisotropies of a specific chiral medium.

Spin-locked enantio-sensitive molecular orientation satisfies the following general set of properties. First, the ensemble-averaged value of \hat{e}^L will have opposite orientations for molecular cations of the same chirality correlated to opposite photoelectron spins along \hat{s}^L . That is, $\langle \hat{e}^L(\hat{s}^L) \rangle = -\langle \hat{e}^L(-\hat{s}^L) \rangle$: the photoelectron spin is locked to the orientation of the cation. Second, $\langle \hat{e}^L \rangle$ will have opposite orientations for the left-handed and right-handed cations correlated to the same direction of the photoelectron spin $\langle \hat{e}_{(R)}^L(\hat{s}^L) \rangle = -\langle \hat{e}_{(S)}^L(\hat{s}^L) \rangle$. Third, $\langle \hat{e}^L \rangle$ will have the same orientation for the left-handed and the right-handed cations correlated to the photoelectrons with opposite spin $\langle \hat{e}_{(R)}^L(\hat{s}^L) \rangle = \langle \hat{e}_{(S)}^L(-\hat{s}^L) \rangle$.

We also propose an experimental protocol able to directly probe spin-chirality coupling in coincidence measurements. Indeed, by detecting electron spin and looking at the averaged orientation of the subset of the cations produced upon ionization by circularly polarised fields and correlated to this spin, one can identify the relative magnitudes of spin torque and Bloch pseu-

dovectors and their relative orientations. When spin torque and Bloch vector are not collinear, the ensemble of cations correlated to a given spin orientation will be oriented in a plane formed by the spin detection axis \hat{s}^L and the axis $\hat{s}^L \times \hat{\Xi}^L$. This is in contrast to MOCD³¹, orienting the molecule around a single axis, that of the photon spin $\hat{\Xi}^L$. Further, since only the spin torque mechanism is sensitive to the spin of the photon, additional opportunity to disentangle and selectively probe the two mechanisms appears in dichroic measurements. Thus, spin-orientation locking offers significant control over the orientation of enantiomers in space, albeit at the expense of quite challenging experimental set-up.

Our geometric formalism lays the foundation for systematic study of non-equilibrium topological effects in gas phase chiral molecules with the opportunity to achieve topological robustness in chiral measurements. Our results open an unexplored path towards understanding both the CISS effect and controlling the interplay of chirality and spin in photo-induced dynamics as well as the enantio-senstive orientation of chiral molecules.

Methods

Synthetic chiral matter

Quantification of spin-chirality coupling in photionization requires a system where both electronic chirality and spin-orbit coupling are rigorously accounted. To this end, we construct chiral electronic densities in an Ar atom corresponding to excitation into a chiral superposition of excited states, resolved on the excited electron spin. The eigenstates and associated spin-resolved pho-

toionization dipole matrix elements of Ar atom were calculated using an atomic configuration-interaction singles treatment^{35–37}:

$$\vec{D}_{I,\vec{k}^M,\mu^M}^M \equiv \langle I \Psi_{\vec{k},\mu^M}^{(-)} | \vec{d}^M | \psi_o \rangle = \langle \psi_{\vec{k},\mu^M}^{(-)} | \langle \chi_{\mu^M} | [\hat{h}_S, \theta(r - r_s)] \sqrt{N} \langle I | (\hat{H}_0 - \epsilon)^{-1} \vec{d}^M | \psi_o \rangle, \quad (14)$$

In Eq. (14), the volume integral in the matrix element is replaced with a surface integral over a sphere of radius r_s where the exact continuum state is matched to the scattering state in the asymptotic region³⁷ and a time integral which has been explicitly evaluated. The resolvent $(\hat{H}_0 - \epsilon)^{-1}$ formally propagates the component of $\vec{d}^M | \psi_o \rangle$ with energy $\epsilon = E_I + k^2/2$ to infinite time, where E_I is the energy of the ion state I , and the projection from the left by $\sqrt{N} \langle I |$ yields an energy-resolved Dyson orbital (N is number of electrons). The commutator of the scattering Hamiltonian \hat{h}_S , i.e., the asymptotic Hamiltonian obeyed by the wave function and the scattering state in the region beyond the matching surface r_s and the Heaviside function $\theta(r - r_s)$ reduces the remaining one-electron volume integral to the surface integral³⁷.

Chiral spin resolved electronic states in Ar are inspired by a similar spinless chiral superposition in the hydrogen atom³⁴, and in the case of hydrogenic wave-functions could be represented as:

$$|\psi_{m,\mu}^{\pm}\rangle = \frac{1}{\sqrt{2}} (|4p_m, \mu\rangle \pm |4d_m, \mu\rangle). \quad (15)$$

Aiming to create analogues of such states in a multielectron system such as the argon atom, we devised an optimization procedure that yields the best approximation to these states (see Appendix A for details).

Bloch vector associated with spin-resolved photoionization

One way to introduce \vec{S} is to consider spin polarization in one-photon ionization from the ground state of a molecule $|\psi_o\rangle$ via circularly polarized light $\vec{E}^L = E_\omega^L(\hat{x}^L + i\varsigma\hat{y}^L)/\sqrt{2}$. Here, E_ω^L is the Fourier component of the incident light at frequency ω , and $\varsigma = \pm 1$ is the dichroic parameter characterising the direction of rotation of the light polarization vector.

We begin by introducing a factorized basis of detector states in the asymptotic region $|I\Psi_{\vec{k},\mu}^{(-)}\rangle = |I\rangle \otimes |\psi_{\vec{k},\mu}^{(-)}\rangle \otimes |\chi_\mu\rangle$. Here, $|I\rangle$ denotes the ionic state, $|\psi_{\vec{k},\mu}^{(-)}\rangle$ denotes the spatial part of the photoelectron wavefunction, and $|\chi_\mu\rangle$ denotes the spin degree of freedom. The detector states $|I\Psi_{\vec{k},\mu}^{(-)}\rangle$ satisfy the orthogonality condition $\langle\Psi_{\vec{k}_1,\mu_1}I'|I\Psi_{\vec{k}_2,\mu_2}\rangle = \delta(\vec{k}_1 - \vec{k}_2)\delta_{\mu_1,\mu_2}\delta_{I,I'}$. These states are then propagated towards the origin using the full Hamiltonian which introduces entanglement between the different ionic channels and spin-resolved photoelectron states, but preserves the orthogonality conditions due to the unitarity of the propagation.

We now consider the full density operator describing the spin and spatial degrees of freedom for ionization into the final photoelectron momentum $k = \sqrt{2E}$ and (degenerate) ion channels I (fixed by the energy conservation):

$$\hat{\varrho}^M = \sum_{I,I'} \int d\Theta_k^M \int d\Theta_{k'}^M \sum_{\mu_1,\mu_2} c_{I,\vec{k},\mu_1}^* c_{I',\vec{k}',\mu_2} |I\Psi_{\vec{k}',\mu_1}\rangle \langle \Psi_{\vec{k},\mu_2} I'|, \quad (16)$$

where, $c_{I,\vec{k},\mu} = i \left(\vec{D}_{I,\vec{k}^M,\mu^M}^L \cdot \vec{E}^L \right)$ is the transition amplitude for ionization, and $\vec{D}_{I,\vec{k}^M,\mu^M}^L$ is the transition dipole matrix element. To obtain the reduced spin-space density matrix, we perform a

partial trace over the spatial continuum states and (degenerate) ionization channels:

$$\varrho_{\mu_1, \mu_2}^M = \text{Tr}_{(\text{spatial+channels})}(\hat{\varrho}^M) = \sum_I \int d\Theta_k^M \langle I\Psi_{\vec{k}, \mu_1} | \hat{\varrho}^M | I\Psi_{\vec{k}, \mu_2} \rangle. \quad (17)$$

Substituting the definition of $\hat{\varrho}^M$, we write:

$$\varrho_{\mu_1, \mu_2}^M = \sum_{I, I'} \sum_{\mu'_1, \mu'_2} \int d\Theta_k^M \int d\Theta_{k'}^M \int d\Theta_{k''}^M c_{I', \vec{k}', \mu'_1}^* c_{I'', \vec{k}'', \mu'_2} \langle I\Psi_{\vec{k}, \mu_1} | I'\Psi_{\vec{k}', \mu'_1} \rangle \langle \Psi_{\vec{k}'', \mu'_2} | I\Psi_{\vec{k}, \mu_2} \rangle. \quad (18)$$

Using the orthogonality relations, the expression simplifies to:

$$\varrho_{\mu_1, \mu_2}^M = \sum_I \int d\Theta_k^M c_{I, \vec{k}, \mu_1}^* c_{I, \vec{k}, \mu_2}. \quad (19)$$

A possible way of introducing the Bloch vector describing spin orientation of a two-level spin 1/2 system defined as $\vec{P} \equiv \text{Tr}(\varrho^M \hat{\Sigma}^M)$ (where, $\hat{\Sigma} = \hat{\sigma}^T$, $\hat{\sigma}$ is the vector of Pauli spin matrices), could be to use ϱ^M with elements given by Eq. (19). In this case the Bloch vector would depend on the properties of the laser field via $c_{I, \vec{k}, \mu_1}, c_{I, \vec{k}, \mu_2}$.

We now introduce the photoionization Bloch vector \vec{S}^M by averaging ϱ_{μ_1, μ_2}^M over random molecular orientations, i.e.,

$$\int d\rho \varrho_{\mu_1, \mu_2}^M = \sum_I \int d\Theta_k^M \left[\int d\rho \left(\vec{D}_{I, \vec{k}^M, \mu_1^M}^L \cdot \vec{E}^L \right)^* \left(\vec{D}_{I, \vec{k}^M, \mu_2^M}^L \cdot \vec{E}^L \right) \right] = \frac{1}{3} |\vec{E}^L|^2 \tilde{\varrho}_{\mu_1, \mu_2}^M \quad (20)$$

where,

$$\tilde{\varrho}_{\mu_1, \mu_2}^M = \sum_I \int d\Theta_k^M \left(\vec{D}_{I, \vec{k}^M, \mu_1}^{M*} \cdot \vec{D}_{I, \vec{k}^M, \mu_2}^M \right). \quad (21)$$

It can be written in equivalent form as

$$\tilde{\varrho}^M = \frac{1}{2} \left(S_0 \mathbb{I} + \vec{S}^M \cdot \hat{\Sigma}^M \right), \quad (22)$$

in which, S_0 is the total ionization rate:

$$S_0 = \sum_I \left[\int d\Theta_k^M \left(\left| \vec{D}_{I,\vec{k}^M, \frac{1}{2}}^M \right|^2 + \left| \vec{D}_{I,\vec{k}^M, -\frac{1}{2}}^M \right|^2 \right) \right] \quad (23)$$

and \vec{S}^M is the photo-ionization Bloch pseudovector in real space

$$\vec{S}^M = \text{Tr} \left(\tilde{\varrho}^M \hat{\Sigma}^M \right). \quad (24)$$

Now, \vec{S}^M is an intrinsic molecular property invariant under rotations of the spin quantization axis provided that these rotations are applied consistently to both the density matrix $\tilde{\varrho}^M$ and the spin operator $\hat{\sigma}^M$.

Spin-resolved geometric field

Spin-resolved geometric field finds its precursor in the concept of geometric magnetism in photoionization³¹ and photoexcitation³² associated with the antisymmetric orbital curvature $\vec{\Omega}$ ³². The curvature $\vec{\Omega}$ quantifies the circular dichroism in photoionization from a superposition of electronic states $|m\rangle, |n\rangle$ in the electric dipole regime^{31,32}. A convenient representation of $\vec{\Omega}$ is via the matrix elements $\vec{\Omega}_{mn}$ of the curvature operator:

$$\hat{F}_a = i\epsilon_{abc}\hat{d}_b\hat{P}_{\mathcal{E}}\hat{d}_c, \quad a, b, c = x, y, z, \quad \vec{\Omega}_{mn} = \langle m|\hat{\vec{F}}|n\rangle, \quad (25)$$

where, ϵ_{abc} denotes the Levi-Cevita symbol, \hat{d} is the dipole operator, and

$$\hat{P}_{\mathcal{E}} = \int d\Theta_k |\psi_{\vec{k}}^{(-)}\rangle\langle\psi_{\vec{k}}^{(-)}|, \quad (26)$$

is the projector on the energy shell, which includes all directions of the photoelectron momentum $\int d\Theta_k$ for a fixed photoelectron energy $\mathcal{E} = k^2/2$ (see also Ref. ³⁸). The operator \hat{F}_a is a time-odd

pseudovector. Thus, $\vec{\Omega}_{nn}$ vanishes for any time-even state n , e.g., the ground state of a molecule that is not resolved on the electron spin ³¹. Therefore, one needs to break time-reversal symmetry to enable the antisymmetric orbital curvature.

One way to do this is to excite a current in molecular bound states prior to photoionization, which creates coherences between the electronic states $|m\rangle, |n\rangle$. In this case, $\vec{\Omega}_{mn}$ will control the enantio-sensitive orientation of the cations leading to the molecular orientation circular dichroism (MOCD) ³¹, which is an example of enantio-sensitive charge directed chemical reactivity ^{31,39}. An alternative way is to resolve photoionization on the photoelectron spin. In this case, we should expect enantio-sensitive molecular orientation to occur even after one-photon ionization from the ground state of a randomly oriented molecule, provided that we distinguish the photoelectron spin.

To explore the interplay of geometry and spin, we introduce the spin-resolved curvature operator $\hat{F}_a^{(\mu_1, \mu_2)}$. In contrast to \hat{F}_a , the operator $\hat{F}_a^{(\mu_1, \mu_2)}$ now involves the fully spin-orbit coupled continuum states $|\Psi_{\vec{k}, \mu}^{(-)}\rangle$ introduced above:

$$\hat{F}_a^{(\mu_1, \mu_2)} = \sum_I i\epsilon_{abc} \hat{d}_b \hat{P}_{I, \mathcal{E}, \mu_1, \mu_2} \hat{d}_c, \quad (27a)$$

$$\hat{P}_{I, \mathcal{E}, \mu_1^M, \mu_2^M} = |I\rangle\langle I| \hat{P}_{\mathcal{E}, \mu_1^M, \mu_2^M}, \quad (27b)$$

$$\begin{aligned} \hat{P}_{\mathcal{E}, \mu_1, \mu_2} &= \int d\Theta_k |\Psi_{\vec{k}, \mu_1}^{(-)}\rangle\langle\Psi_{\vec{k}, \mu_2}^{(-)}| \\ &= \int d\Theta_k \begin{bmatrix} |\Psi_{\vec{k}, \frac{1}{2}}^{(-)}\rangle\langle\Psi_{\vec{k}, \frac{1}{2}}^{(-)}| & |\Psi_{\vec{k}, \frac{1}{2}}^{(-)}\rangle\langle\Psi_{\vec{k}, -\frac{1}{2}}^{(-)}| \\ |\Psi_{\vec{k}, -\frac{1}{2}}^{(-)}\rangle\langle\Psi_{\vec{k}, \frac{1}{2}}^{(-)}| & |\Psi_{\vec{k}, -\frac{1}{2}}^{(-)}\rangle\langle\Psi_{\vec{k}, -\frac{1}{2}}^{(-)}| \end{bmatrix}_{\mu_1, \mu_2}. \end{aligned} \quad (27c)$$

The spin-resolved curvature operators give rise to the curvature pseudovectors:

$$\vec{\Omega}_{m,n}^{(\mu_1,\mu_2)} \equiv \langle m | \hat{\vec{F}}^{(\mu_1,\mu_2)} | n \rangle. \quad (28)$$

Since we consider photoionization from a single state, e.g., ground state of a molecule, we will drop the indices m, n labeling the ionizing state as $m = n$ (see Appendix B). The curvature pseudovectors $\vec{\Omega}^{(\mu_1,\mu_2)}$ are the elements of a matrix Ω in spin space: $(\Omega)_{\mu_1,\mu_2} \equiv \vec{\Omega}^{(\mu_1,\mu_2)}$. The matrix Ω is an operator in spin space, which represents an effective spin-dependent geometric field. We demonstrate that this field can cause both non-enantio-sensitive spin orientation due to the spin geometric susceptibility scalar χ_{gs} and impart a torque $\vec{\tau}$ on electron spin leading to enantio-sensitive orientation.

Momentum and spin resolved ionization rate

The ionization rate for a given orientation is obtained by projecting the full wavefunction in the asymptotic region onto the spin detection axis \hat{s}^L acting on $|\chi_{\mu^M}\rangle$ and onto the asymptotic states $|\psi_{\vec{k}^M,\mu^M}^{(-)}\rangle$ and ionic states $|I\rangle$ with energy \mathcal{E} via the projectors

$$\hat{P}_{\hat{s}^L} = \frac{1}{2} (\mathbb{I} + \hat{s}^L \cdot \hat{\sigma}^L), \quad (29)$$

$$\hat{P}_{\mathcal{E}} = \sum_{\mu} |\psi_{\vec{k},\mu}^{(-)}\rangle \langle \psi_{\vec{k},\mu}^{(-)}| \sum_I |I\rangle \langle I|. \quad (30)$$

Note that spatial projection is limited to the asymptotic region. Performing the necessary operations, we obtain

$$W^M(\hat{\vec{k}}^M, \hat{s}^L, \rho) = \frac{1}{2} \sum_{I,\mu_1^M,\mu_2^M} \left(\vec{D}_{I,\vec{k}^M,\mu_1^M}^{L*} \cdot \vec{E}^{L*} \right) \left(\vec{D}_{I,\vec{k}^M,\mu_2^M}^L \cdot \vec{E}^L \right) \left(\delta_{\mu_1^M,\mu_2^M} + \hat{s}^L \cdot \hat{\sigma}_{\mu_1^M,\mu_2^M}^L \right), \quad (31)$$

which follows from the orthogonality relation $\langle \Psi_{\vec{k}_1, \mu_1}^{(-)} | \Psi_{\vec{k}_2, \mu_2}^{(-)} \rangle = \delta(\vec{k}_1 - \vec{k}_2) \delta_{\mu_1, \mu_2}$. We have also introduced vector $\hat{\sigma}_{\mu_1^M, \mu_2^M}^L = \langle \chi_{\mu_1^M} | \hat{\sigma}^L | \chi_{\mu_2^M} \rangle$ (see Appendix C).

Geometric spin susceptibility

In the one photon regime, the average spin orientation $\langle \hat{s}^L \rangle$ is aligned with the laboratory-frame photon spin direction $\hat{\Xi}^L$, with a magnitude determined by the scalar contraction $\frac{1}{3S_0} \text{Tr} (\hat{\Sigma}^M \cdot \Omega^M)$. This structure is reminiscent that of standard magnetic susceptibility, where the spin response to an external magnetic field is characterized by $\langle \vec{s} \rangle = \chi \vec{B}$. Here, however, the role of the external field is replaced by the fixed direction of photon spin, and the response arises from the intrinsic geometry of the photoionization dipoles, encoded in the spin-resolved curvature field Ω^M . Accordingly, the dimensionless scalar

$$\chi_{gs} := \frac{1}{3S_0} \text{Tr} (\hat{\Sigma}^M \cdot \Omega^M)$$

may be interpreted as a *geometric spin susceptibility*—a measure of how geometric structure mediates spin orientation in response to circularly polarised light.

Formally χ_{gs} is obtained as the average value of \hat{s}^L , i.e.,

$$\langle \hat{s}^L \rangle = \frac{\int d\Theta_s^L \int d\Theta_k^M W^M(\hat{k}^M, \hat{s}^L, \rho) \hat{s}^L}{\int d\Theta_s^L \int d\Theta_k^M W^M(\hat{k}^M, \hat{s}^L, \rho)} = \frac{1}{3S_0} \text{Tr} (\hat{\Sigma}^M \cdot \Omega^M) \hat{\Xi}^L \equiv \chi_{gs} \hat{\Xi}^L, \quad (32)$$

where, $\hat{\Xi}^L = -(i \vec{E}^{L*} \times \vec{E}^L) / |E_\omega^L|^2 = \varsigma \hat{z}^L$ is the direction of photon spin (see Appendix D for details). Here the trace is performed over the spin space, therefore, Eq. (32) yields a result that is independent of the chosen spin quantization axis or spin basis. Hence, the curvature operator in spin space Ω^M orients the spin $\hat{\Sigma}^M$ in spin space by biasing spin orientations oriented along

spin-dependent geometric field.

With some effort, one can show that Eq. (32) is algebraically equivalent to the coefficient A introduced by Cherepkov². Although structurally cumbersome, Cherepkov's original expression remains an important point of reference. In contrast, Eq. (32), as derived here, exposes the geometric origin of spin polarization in photoionization: the spin-dependent geometric field associated with photoionization acts to orient the photoelectron spin.

Equation (32) represents an anomalous (curvature-driven) vectorial observable analogous to Class I observables introduced in Ref. ³¹. Ref. ⁴⁴ has experimentally detected this observable in the case of multiphoton ionization and it has been also detected in atomic targets in the one-photon case ⁴⁵. See Appendix F for the case of synthetic chiral Argon considered here.

O.S., A.F. O. and P.C.F. acknowledge ERC-2021-AdG project ULISSES, grant agreement No 101054696. A.F.O. acknowledges funding from the Royal Society URF/R1/201333, URF/ERE/210358, and URF/ERE/231177.

²See Eq. 20 of Ref. ⁴⁰ and Eq. 7 of Ref. ⁴¹ which was used by Cherepkov. The readers are directed to Refs. ^{42,43} which explore complementarities between these two approaches.

Appendices

A Chiral superpositions of Argon excited states

The excited states of argon have good quantum numbers J and M_J , when considering spin–orbit interaction:

$$\hat{H}_0 |w\rangle = E_w |w\rangle, \quad \hat{J}^2 |w\rangle = J(J+1) |w\rangle, \quad \hat{J}_z |w\rangle = M_J |w\rangle. \quad (33)$$

In a close-coupling description of the excited states, the active electron is *entangled* with the ion. In the particle–hole basis employed in configuration-interaction singles ^{35,36}, the excited states have contributions from multiple ion channels:

$$|w\rangle = \sum_i \hat{\mathcal{A}}(\hat{a}_i |\Phi_0\rangle) |\chi_i\rangle, \quad (34)$$

where $|\Phi_0\rangle$ is the Hartree–Fock reference state (the ground state), \hat{a}_i annihilates the i th occupied orbital, $|\chi_i\rangle$ is the channel-specific orbital for the excited or free electron, and $\hat{\mathcal{A}}$ is the antisymmetrization operator. $\hat{a}_i |\Phi_0\rangle$ is thus an approximation to the state of the ion (Koopman’s approximation), and the orbitals of $\hat{a}_i |\Phi_0\rangle$ and $|\chi_i\rangle$ are expanded in the $\ell j m_j$ basis, wherein the spin–orbit interaction is diagonal. In our calculations, relativistic effects (of which the spin–orbit interaction is one), are treated using a relativistic effective-core potential ⁴⁶ (there are alternative approaches described in the literature ^{47–49}, but for our purposes, the present approach is more suitable).

For each excited state $|w\rangle$, we may compute the ionization dipole matrix elements $\langle I \vec{k} m_s | \hat{d} | w \rangle$, using a surface-flux technique ^{35,37}, and they are resolved on the ion state I and the photoelectron

state in terms of the magnitude $k = |\vec{k}|$ of the linear momentum, the angular distribution in terms of the orbital angular momentum $(\ell m_\ell)_{\vec{k}}$, and the spin m_s .

We however desire the ionization dipole matrix elements starting from a chiral superposition of states which as far as possible resemble one-electron excited states characterized by $n \ell m_\ell s m_s$, i.e. our desired initial wavefunction is given by

$$|\Psi\rangle = |\Psi_{\text{ion}}\rangle \left[\sum_i f_i |(n \ell m_\ell s m_s)_i\rangle \right] \stackrel{\text{def}}{=} |\Psi_{\text{ion}}\rangle \sum_i f_i |k_i\rangle, \quad (35)$$

where the ionic state $|\Psi_{\text{ion}}\rangle$ is shared between all terms in the expansion, and the expansion coefficients f_i may be chosen at will. In the second step, we have introduced a short-hand notation for the state of the electron.

To achieve this goal, we proceed in two steps:

1. Find linear combinations of the true excited states $|w\rangle$ that are approximately factorized into an ionic part and an electronic part:

$$|\Phi_i\rangle \approx |\Phi_{\text{ion},i}\rangle |k_i\rangle. \quad (36)$$

There will be multiple such approximate factorizations, since there are multiple ionization channels. Below, we discuss how we try to find the “optimal” ones.

2. Given a set $\{|k_i\rangle, a_i\}$, try to find linear combinations of the factorized states (36), that simultaneously are as close to the desired chiral superposition as possible, while still maintaining maximum overlap of the ionic wavefunction, since that increases the purity of the state.

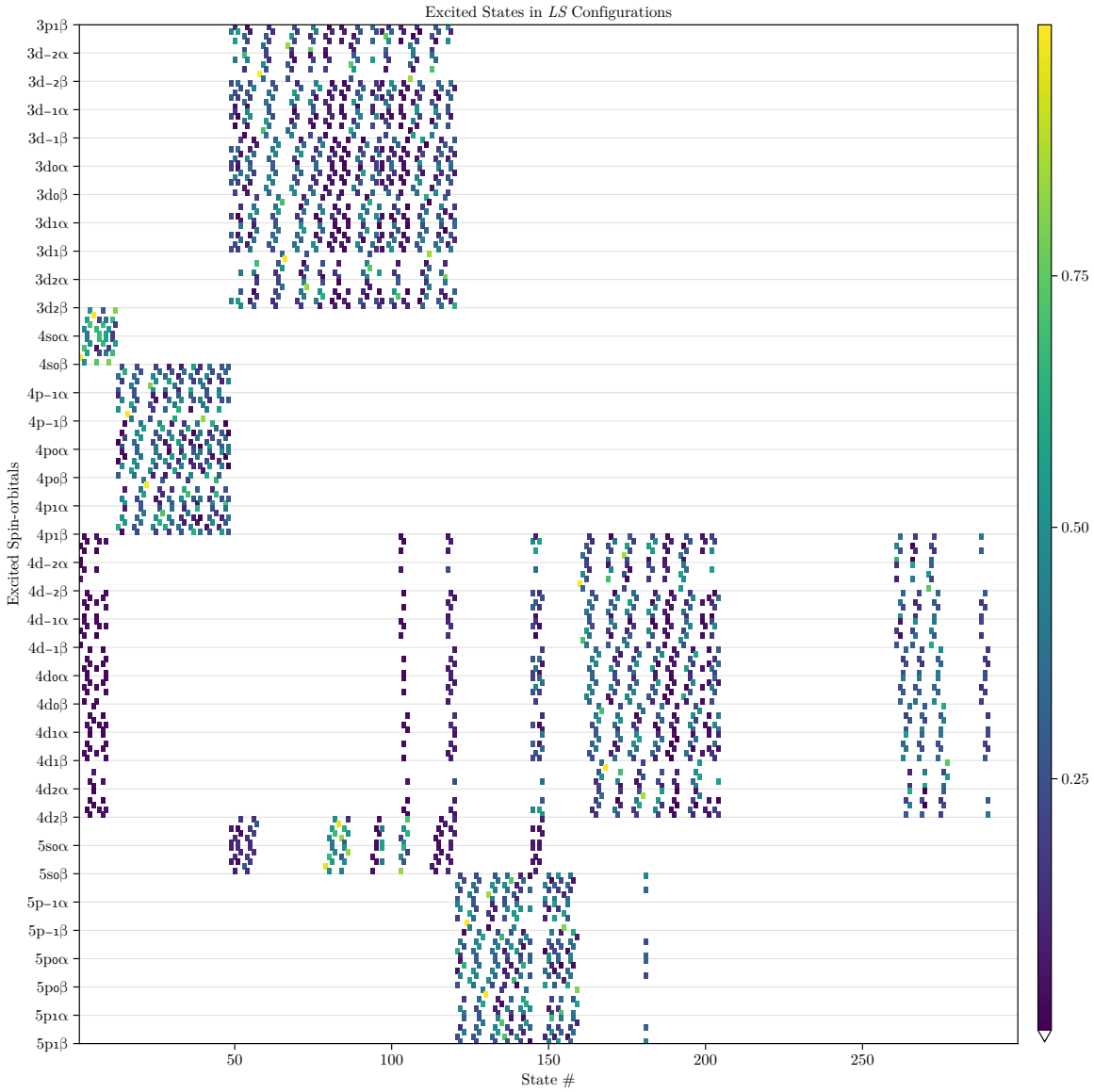


Figure 7: Overlaps between excited states and spin-configurations, i.e. uncoupled configurations of spin-orbitals in the $n\ell m_\ell s m_s$ basis. The spin-configurations (the y axis) are ordered by the quantum numbers of the excited spin-orbital, given as labels pertaining to the block immediately above them. It is clearly visible that this overlap matrix is mostly composed of disjoint blocks, where the excited states accurately classified by $n\ell$ of the excited spin-orbital.

State Factorization by Block Diagonalization in Orthogonal Subspaces We define the matrix B with matrix elements $b_{vw} \stackrel{\text{def}}{=} \langle v|w\rangle$, which is the projection of the true excited state $|w\rangle$ given by (33) on the *uncoupled* configuration $|v\rangle$ in the $\ell m_\ell s m_s$ basis. We may permute the rows and columns of the matrix B , such that it consists of mostly disjoint blocks B_b , which we can transform separately (see Fig. 7). This is possible since the quantum numbers of the excited electron are *almost* good quantum numbers. E.g. a $4s_0\alpha$ state, will contain contributions from $4d_{m_\ell}\alpha$ configurations, but they will be of less importance, compared to the dominant configurations.

The rows in each block B_b are ordered such that they are grouped by the excited orbital, and we then wish to apply a transformation to B_b such that it becomes approximately block diagonal, i.e. we find expansions for states with a particular excited orbital (in the $\ell m_\ell s m_s$ basis) in terms of the true excited states (in the $\ell j m_j$ basis). This achieves the approximate factorization (36), thereby disentangling the states. It will however introduce an energy spread, i.e. the factorized states are no longer stationary states of the Hamiltonian.

We consider without loss of generality a case with two different excited orbitals $|k_p\rangle$ and $|k_q\rangle$ (e.g. $4s_0\alpha$ and $4s_0\beta$), and drop the b subscript for brevity. The overlap matrix (within this block) is then given by

$$B = (\hat{P} + \hat{Q})B(\hat{P} + \hat{Q}), \quad (37)$$

where \hat{P} projects on the configurations containing $|k_p\rangle$ and \hat{Q} on configurations containing $|k_q\rangle$.

Within the chosen space, $\hat{P} + \hat{Q} = \hat{\mathbf{1}}$. We wish to find a unitary matrix U , such that

$$\begin{cases} \hat{P}UB\hat{Q} = 0, \\ \hat{Q}UB\hat{P} = 0, \end{cases} \quad (38)$$

i.e. a block-diagonalizing transform. We will not be able to achieve this identically, therefore we formulate it as a minimization problem:

$$\min_U \|\hat{P}UB\hat{Q}\|^2 + \|\hat{Q}UB\hat{P}\|^2 \quad (39)$$

such that $U^\dagger U = \hat{\mathbf{1}}$.

Its equivalent Lagrangian formulation, incorporating the unitarity constraint on U using a Lagrangian multiplier λ , is given by

$$\begin{aligned} \hat{L} &= \text{tr}(\hat{Q}^\dagger B^\dagger U^\dagger \hat{P}^\dagger \hat{P}UB\hat{Q}) + \text{tr}(\hat{P}^\dagger B^\dagger U^\dagger \hat{Q}^\dagger \hat{Q}UB\hat{P}) + \lambda[\text{tr}(U^\dagger U) - 1] \\ &= \text{tr}(\hat{Q}^\dagger B^\dagger U^\dagger \hat{P}UB\hat{Q}) + \text{tr}(\hat{P}^\dagger B^\dagger U^\dagger \hat{Q}UB\hat{P}) + \lambda[\text{tr}(U^\dagger U) - 1] \\ &= \text{tr}(B\hat{Q}B^\dagger U^\dagger \hat{P}U) + \text{tr}(B\hat{P}B^\dagger U^\dagger \hat{Q}U) + \lambda[\text{tr}(U^\dagger U) - 1], \end{aligned} \quad (40)$$

where we have used the cyclic property of the trace operation, the fact that $\hat{P}^\dagger \hat{P} = \hat{P}^2 = \hat{P}$, and similarly for \hat{Q} . Variation of \hat{L} with respect to U^\dagger , and λ , respectively, yields

$$\begin{aligned} \delta_{U^\dagger} \hat{L} &= B\hat{Q}B^\dagger \hat{P}U + B\hat{P}B^\dagger \hat{Q}U + \lambda U = (B\hat{Q}B^\dagger \hat{P} + B\hat{P}B^\dagger \hat{Q} + \lambda \hat{\mathbf{1}})U, \\ \delta_\lambda \hat{L} &= U^\dagger U - \hat{\mathbf{1}}, \end{aligned} \quad (41)$$

which we recognize as an eigenvalue problem. The minimization problem (40) may be solved using any standard non-linear solver; its variation (41) can be used to improve convergence. In our implementation, however, we employ Riemannian manifold optimization ⁵⁰ of the minimization problem (39) as-is; the matrix U is required to stay on the *Stiefel* manifold, i.e. the matrix manifold

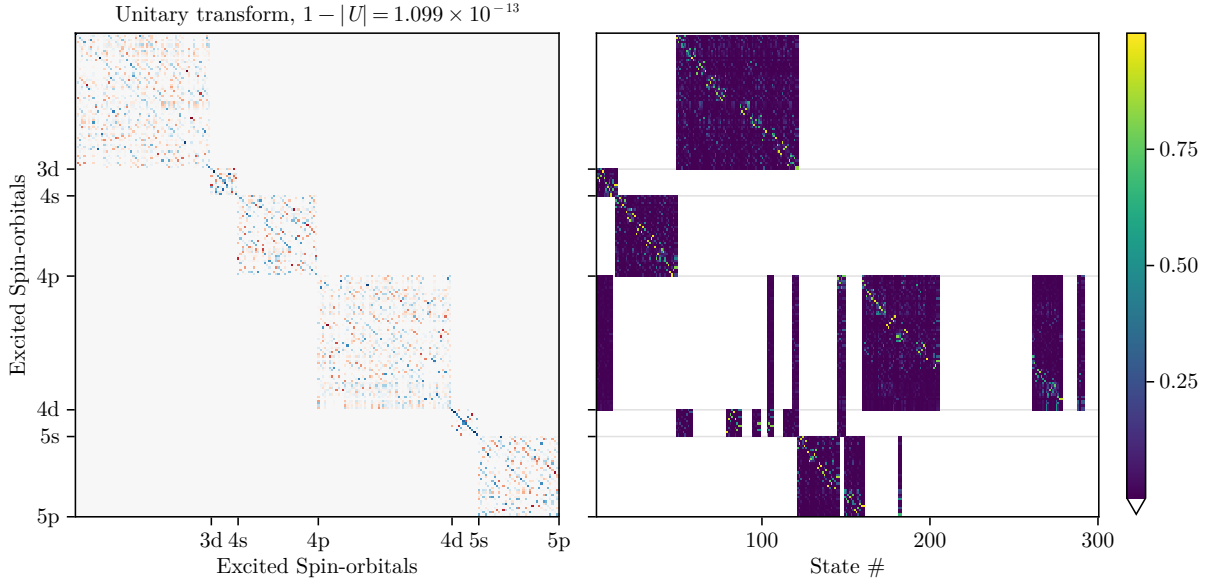


Figure 8: The left panel shows the optimized unitary transform matrix U . The right panel shows the overlap matrix UB between rotated excited states and the spin-configurations, again grouped by the excited spin-orbitals.

of matrices with mutually orthonormal columns. In Fig. 8, the optimized U is shown, together with the transformed overlap matrix UB .

With this method, we are able to achieve factorizations that to $\geq 80\%$ have the excited electron in the desired spin-orbital $n\ell m_\ell s m_s$, with some residual contamination from other states; see Fig. 9 for the subspace of 4p states. The energy spread is typically small: $(\langle E^2 \rangle - \langle E \rangle^2)^{1/2} \lesssim 10^{-2} \langle E \rangle$, with the excited states of interest having energies $\langle E \rangle \gtrsim 0.4$ Ha.

Deriving Chiral Superpositions As we saw above (e.g. in Fig. 9), there are multiple states that have the excited electron in the same spin-orbital $|k_i\rangle$. Any of these states may be written as a

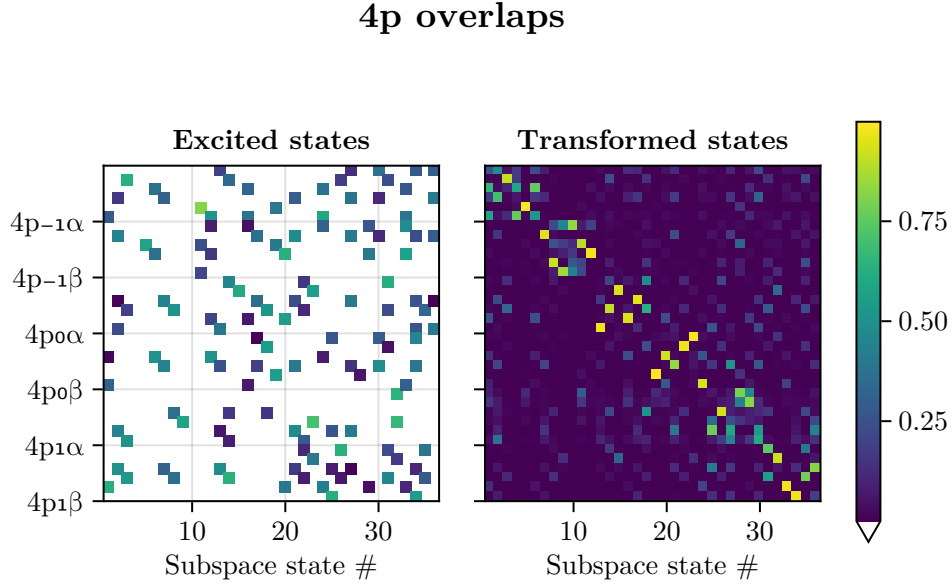


Figure 9: The left panel shows the overlaps between the excited states which are dominated by excited electrons in 4p orbitals, resolved on the individual spin-orbitals. The right panel the resultant states after applying the unitary transform U within this subspace. As can be seen, the block-diagonalization is not perfect. Additionally, we have multiple transformed states for each spin-orbital.

linear combination of the true excited states (33):

$$|\Phi_i\rangle_j = \sum_w c_{jw}^{(i)} |w\rangle = \hat{\mathcal{A}} \left[\sum_w c_{jw}^{(i)} \hat{a}_{k_i} |w\rangle \right] |k_i\rangle \implies |\vec{\Phi}_i\rangle = C_i |\vec{w}\rangle = \hat{\mathcal{A}} [C_i \hat{a}_{k_i} |\vec{w}\rangle] |k_i\rangle, \quad (42)$$

where $|\Phi_i\rangle_j$ is the j th state with the excited electron in the spin-orbital $|k_i\rangle$, $c_{jw}^{(i)}$ the corresponding expansion coefficient for the true eigenstate $|w\rangle$. We also introduce the vector notation $|\vec{\Phi}_i\rangle^T \stackrel{\text{def}}{=} \begin{bmatrix} |\Phi_i\rangle_1 & |\Phi_i\rangle_2 & \dots \end{bmatrix}^T$, and similarly for $|\vec{w}\rangle$. C_i are the corresponding expansion coefficients ar-

ranged into a matrix. In the second step we have written the states on the factorized form (36).

If we now wish to create a chiral superposition of the excited electron, i.e. we wish to define our initial state according to

$$|\Psi_0\rangle = |\Psi_{\text{ion}}\rangle \sum_i f_i |k_i\rangle, \quad (43)$$

for every $|k_i\rangle$ we need to make a linear combination of the possible $|\Phi_i\rangle_j$ such that the ion degrees-of-freedom maximally overlap; otherwise the factorization (43) does not hold. Symbolically, we write this as

$$\left| \vec{g}_i \cdot \vec{\Phi}_i \right\rangle = \vec{g}_i^H C_i |\vec{w}\rangle = \hat{\mathcal{A}} [\vec{g}_i^H C_i \hat{a}_{k_i} |\vec{w}\rangle] |k_i\rangle. \quad (44)$$

To achieve the desired factorized state (43), we thus have to solve the following maximization problem:

$$\max_G [\vec{g}_i^H C_i \hat{a}_{k_i} |\vec{w}\rangle]^H [\vec{g}_j^H C_j \hat{a}_{k_j} |\vec{w}\rangle] = \max_G [\langle \vec{w} | \hat{a}_{k_i}^\dagger C_i^H \vec{g}_i] [\vec{g}_j^H C_j \hat{a}_{k_j} |\vec{w}\rangle], \quad (45)$$

such that $\|\vec{g}_i\|^2 = 1, \forall i,$

where the i th column of the matrix G is the vector \vec{g}_i .

B Time parity

The incoming scattering states are related to outgoing scattering states via the full S-matrix, which may mix spin components:

$$|\Psi_{\vec{k},\mu}^{(-)}\rangle = \sum_{\mu'} \int d\Theta_{\vec{k}'} |\Psi_{\vec{k}',\mu'}^{(+)}\rangle S_{\vec{k}',\mu';\vec{k},\mu}. \quad (46)$$

Taking the Hermitian adjoint

$$\langle \Psi_{\vec{k},\mu}^{(-)} | = \sum_{\mu'} \int d\Theta_{\vec{k}'} S_{\vec{k}',\mu';\vec{k},\mu}^* \langle \Psi_{\vec{k}',\mu'}^{(+)} |, \quad (47)$$

while the projector onto all incoming scattering states at fixed energy \mathcal{E} is taken by summing over the spin projection μ , and is given by:

$$\hat{P}_{\mathcal{E}}^{(-)} = \sum_{\mu} \int d\Theta_{\vec{k}} |\Psi_{\vec{k},\mu}^{(-)}\rangle \langle \Psi_{\vec{k},\mu}^{(-)}|. \quad (48)$$

Substituting Eqs. (46) and (47) into Eq. (48), we find:

$$\begin{aligned} \hat{P}_{\mathcal{E}}^{(-)} &= \sum_{\mu} \int d\Theta_{\vec{k}} \left(\sum_{\mu'} \int d\Theta_{\vec{k}'} |\Psi_{\vec{k}',\mu'}^{(+)}\rangle S_{\vec{k}',\mu';\vec{k},\mu} \right) \left(\sum_{\mu''} \int d\Theta_{\vec{k}''} S_{\vec{k}'',\mu'';\vec{k},\mu}^* \langle \Psi_{\vec{k}'',\mu''}^{(+)} | \right) \\ &= \sum_{\mu',\mu''} \int d\Theta_{\vec{k}'} d\Theta_{\vec{k}''} |\Psi_{\vec{k}',\mu'}^{(+)}\rangle \left(\sum_{\mu} \int d\Theta_{\vec{k}} S_{\vec{k}',\mu';\vec{k},\mu} S_{\vec{k}'',\mu'';\vec{k},\mu}^* \right) \langle \Psi_{\vec{k}'',\mu''}^{(+)} |. \end{aligned} \quad (49)$$

Using unitarity of the full S-matrix on the energy shell, i.e.,

$$\sum_{\mu} \int d\Theta_{\vec{k}} S_{\vec{k}',\mu';\vec{k},\mu} S_{\vec{k}'',\mu'';\vec{k},\mu}^* = \delta_{\mu'\mu''} \delta(\Theta_{\vec{k}'} - \Theta_{\vec{k}''}), \quad (50)$$

we recover

$$\hat{P}_{\mathcal{E}}^{(-)} = \sum_{\mu} \int d\Theta_{\vec{k}} |\Psi_{\vec{k},\mu}^{(+)}\rangle \langle \Psi_{\vec{k},\mu}^{(+)}| = \hat{P}_{\mathcal{E}}^{(+)}. \quad (51)$$

Thus, the projectors onto the energy shell constructed from incoming and outgoing states are equal:

$$\hat{P}_{\mathcal{E}}^{(-)} = \hat{P}_{\mathcal{E}}^{(+)}. \quad (52)$$

Now we can explore time parity of curvature operator $\hat{\mathbb{F}} = (\hat{\mathbb{F}}^{\frac{1}{2}}, \hat{\mathbb{F}}^{\frac{1}{2}, -\frac{1}{2}})$. Let \hat{T} be the time-reversal operator which is anti-unitary, i.e., $\hat{T}(c_1|\alpha\rangle + c_2|\beta\rangle) = c_1^*|\tilde{\alpha}\rangle + c_2^*|\tilde{\beta}\rangle$ where, the tilde denotes the time-reversed state. A Hermitian operator \hat{A} is either time-even (+1) or time-odd

(−1) when $\hat{T}\hat{A} = \pm\hat{A}\hat{T}$. For a spin-1/2 system, the time-reversal operator satisfies the condition $\hat{T}^2 = -\mathbb{I}$, and therefore acts on the spin degree of freedom $|\chi_{\pm\frac{1}{2}}\rangle$ as $\hat{T}|\chi_{\pm\frac{1}{2}}\rangle = \pm\eta|\chi_{\mp\frac{1}{2}}\rangle$ where η is an arbitrary phase. Applying the time-reversal operator \hat{T} to the spin-symmetric curvature, and taking into account that \hat{T} flips the spin we obtain:

$$\begin{aligned}\hat{T}\left(\hat{F}_{+,a}|\phi\rangle\right) &= \hat{T}\left[i\epsilon_{abc}\hat{d}_b\left(\frac{\hat{P}_{\mathcal{E},\frac{1}{2},\frac{1}{2}}^{(-)} + \hat{P}_{\mathcal{E},-\frac{1}{2},-\frac{1}{2}}^{(-)}}{2}\right)\hat{d}_c|\phi\rangle\right] = \hat{T}\left[i\epsilon_{abc}\hat{d}_b\left(\frac{1}{2}\sum_{\mu}\hat{P}_{\mathcal{E},\mu,\mu}^{(-)}\right)\hat{d}_c|\phi\rangle\right] \\ &= \hat{T}\left[\frac{1}{2}i\epsilon_{abc}\hat{d}_b\hat{P}_{\mathcal{E}}^{(-)}\hat{d}_c|\phi\rangle\right] = -\frac{1}{2}i\epsilon_{abc}\hat{d}_b\hat{P}_{\mathcal{E}}^{(+)}\hat{d}_c\hat{T}|\phi\rangle = -\hat{F}_{+,a}\hat{T}|\phi\rangle\end{aligned}\quad (53)$$

(The ion index does not affect the results and is suppressed for simplicity). Thus, the operator $\hat{F}_{+,a}$ is time-odd. Meanwhile, the operator $\hat{F}_a^{(\mu_1,\mu_2)}$ is, in general, neither time-odd nor time-even since $\hat{P}_{\mathcal{E},\mu}^{(-)} \neq \hat{P}_{\mathcal{E},\mu}^{(+)}$. This property enables non-zero diagonal matrix elements of the curvature operator $\vec{\Omega}_{m,n}^{(\mu_1,\mu_2)}$ in all bound states, including the ground state of a molecule.

C Ionization rate for a given molecular orientation

Using perturbation theory, the full spinor valued electron wave-function at the end of the ionizing pulse can be written as

$$|\psi\rangle = |\psi_o\rangle + \sum_{I,\mu^M} \int d\Theta_k^M c_{I,\vec{k}^M,\mu^M} |I\Psi_{\vec{k}^M,\mu^M}^{(-)}\rangle, \quad (54a)$$

$$c_{I,\vec{k}^M,\mu^M} = i \left(\vec{D}_{I,\vec{k}^M,\mu^M}^L \cdot \vec{E}^L \right) \quad (54b)$$

where $|\psi_o\rangle$ is the ground state of the molecule, I denotes the ionic channel, $|\Psi_{\vec{k}^M,\mu^M}^{(-)}\rangle$ is the fully spin-coupled continuum state with momentum \vec{k}^M . In the asymptotic region $|\Psi_{\vec{k}^M,\mu^M}^{(-)}\rangle = |\psi_{\vec{k}^M,\mu^M}^{(-)}\rangle |\chi_{\mu^M}\rangle$, where $\mu^M = \pm\frac{1}{2}$ is the spin projection on the z-axis of the molecular frame in the

asymptotic region. The transition dipole matrix element in the laboratory frame is $\vec{D}_{I,\vec{k}^M,\mu^M}^L \equiv \langle I\Psi_{\vec{k}^M,\mu^M}^{(-)} | \vec{d}^L | \psi_o \rangle$ (see Eq.(14) for details), and the laser field is $\vec{E}^L = E_\omega^L (\hat{x}^L + i\varsigma \hat{y}^L)/\sqrt{2}$, where E_ω^L is the laser field Fourier component at frequency ω and $\varsigma = \pm 1$ is the dichroic parameter characterising the direction of rotation of the light polarization vector.

The spin and momentum resolved photoionization rate for a given orientation is obtained in the asymptotic region by projecting $|\chi_{\mu^M}\rangle$ from the molecular z-axis onto the spin detection axis \hat{s}^L in the laboratory frame via

$$\hat{P}_{\hat{s}^L} = \frac{1}{2} (\mathbb{I} + \hat{s}^L \cdot \hat{\sigma}^L). \quad (55)$$

Here $\hat{\sigma}^L$ is the vector of Pauli spin matrices

$$\hat{\sigma}^L = \begin{bmatrix} 0 & 1 \\ 1 & 0 \end{bmatrix} \hat{\xi}^L + \begin{bmatrix} 0 & -i \\ i & 0 \end{bmatrix} \hat{\eta}^L + \begin{bmatrix} 1 & 0 \\ 0 & -1 \end{bmatrix} \hat{\zeta}^L. \quad (56)$$

Next, $|\psi\rangle$ is projected in the asymptotic region onto the asymptotic scattering states and ionic states with fixed total energy \mathcal{E} by taking the contributions of the spin-up and down photoelectrons as well as final ion states via

$$\hat{P}_\mathcal{E} = \sum_I \sum_{\mu^M=\pm\frac{1}{2}} (|\chi_{\mu^M}\rangle \langle \chi_{\mu^M}|) \otimes \left(|I\Psi_{\vec{k}^M,\mu^M}^{(-)}\rangle \langle I\Psi_{\vec{k}^M,\mu^M}^{(-)}| \right). \quad (57)$$

Performing the necessary operations, we get

$$\begin{aligned} W^M(\hat{\mathbf{k}}^M, \hat{\mathbf{s}}^L, \rho) &= \langle \psi | \hat{P}_\mathcal{E} \hat{P}_{\hat{s}^L} | \psi \rangle \\ &= \sum_{I,I_1,I_2} \sum_{\mu^M, \mu_1^M, \mu_2^M} \int d\Theta_{k_1}^M \int d\Theta_{k_2}^M c_{I_1, \vec{k}_1^M, \mu_1^M}^* c_{I_2, \vec{k}_2^M, \mu_2^M} \\ &\quad \langle I_1 \Psi_{\vec{k}_1^M, \mu_1^M}^{(-)} | \langle \chi_{\mu_1^M} | \left[(|\chi_{\mu^M}\rangle \langle \chi_{\mu^M}|) \otimes \left(|I\Psi_{\vec{k}^M, \mu^M}^{(-)}\rangle \langle I\Psi_{\vec{k}^M, \mu^M}^{(-)}| \right) \otimes \left(\frac{\mathbb{I} + \hat{s}^L \cdot \hat{\sigma}^L}{2} \right) \right] |I_2 \Psi_{\vec{k}_2^M, \mu_2^M}^{(-)} \rangle | \chi_{\mu_2^M} \rangle \end{aligned}$$

$$= \frac{1}{2} \sum_{I, \mu_1^M, \mu_2^M} \left(\vec{D}_{I, \vec{k}^M, \mu_1^M}^{L*} \cdot \vec{E}^{L*} \right) \left(\vec{D}_{I, \vec{k}^M, \mu_2^M}^L \cdot \vec{E}^L \right) \left(\delta_{\mu_1^M, \mu_2^M} + \hat{\mathbf{s}}^L \cdot \hat{\boldsymbol{\sigma}}_{\mu_1^M, \mu_2^M}^L \right). \quad (58)$$

The last line follows from the orthogonality relation $\langle \Psi_{\vec{k}_1, \mu_1}^{(-)} | \Psi_{\vec{k}_2, \mu_2}^{(-)} \rangle = \delta(\vec{k}_1 - \vec{k}_2) \delta_{\mu_1, \mu_2}$. We have also introduced vector $\hat{\boldsymbol{\sigma}}_{\mu_1^M, \mu_2^M}^L = \langle \chi_{\mu^M} | \hat{\boldsymbol{\sigma}}^L | \chi_{\mu^M} \rangle$, i.e.,

$$\hat{\boldsymbol{\sigma}}_{\pm \frac{1}{2}, \pm \frac{1}{2}}^L = \pm \hat{\boldsymbol{\zeta}}^L, \quad \hat{\boldsymbol{\sigma}}_{\pm \frac{1}{2}, \mp \frac{1}{2}}^L = \hat{\boldsymbol{\xi}}^L \mp i \hat{\boldsymbol{\eta}}^L = \hat{\boldsymbol{\sigma}}_{\mp \frac{1}{2}, \pm \frac{1}{2}}^*. \quad (59)$$

D Orientation-averaging

The main results of the paper will involve the orientation-averaged value of $W^M(\hat{\mathbf{k}}^M, \hat{\mathbf{s}}^L, \rho)$, i.e.,

$$\int d\rho W^M(\hat{\mathbf{k}}^M, \hat{\mathbf{s}}^L, \rho) = \frac{1}{2} \sum_{I, \mu_1^M, \mu_2^M} \int d\rho \left(\vec{D}_{I, \vec{k}^M, \mu_1^M}^{L*} \cdot \vec{E}^{L*} \right) \left(\vec{D}_{I, \vec{k}^M, \mu_2^M}^L \cdot \vec{E}^L \right) \left(\delta_{\mu_1^M, \mu_2^M} + \hat{\mathbf{s}}^L \cdot \hat{\boldsymbol{\sigma}}_{\mu_1^M, \mu_2^M}^L \right). \quad (60)$$

where, the orientation $\rho \equiv \alpha\beta\gamma$ is defined by the Euler angles in the zyz-convention, where $\int d\rho \equiv \frac{1}{8\pi^2} \int_0^{2\pi} d\alpha \int_0^\pi d\beta \sin\beta \int_0^{2\pi} d\gamma$. Now, Eq. (58) fixes the photoelectron momentum and spin-detection axis in the molecular and laboratory frame, respectively, in order to simplify the evaluation of Eq. (60). By doing so, the transition dipole matrix element in the molecular frame $\vec{D}_{I, \vec{k}^M, \mu^M}^M$ will not have any argument that depends on the orientation ρ , and can therefore be trivially rotated into the lab frame:

$$\vec{D}_{I, \vec{k}^M, \mu^M}^L = \langle I\Psi_{\vec{k}^M, \mu^M}^{(-)} | \vec{d}^L | \psi_o \rangle = \langle I\Psi_{\vec{k}^M, \mu^M}^{(-)} | R_\rho \vec{d}^M | \psi_o \rangle = R_\rho \langle I\Psi_{\vec{k}^M, \mu^M}^{(-)} | \vec{d}^M | \psi_o \rangle = R_\rho \vec{D}_{I, \vec{k}^M, \mu^M}^M. \quad (61)$$

Meanwhile, by fixing the spin-detection axis in the lab frame, the spin projection operator $\hat{P}_{\hat{\mathbf{s}}} = (\mathbb{I} + \hat{\mathbf{s}}^L \cdot \hat{\boldsymbol{\sigma}}^L)/2$ essentially rotates the direction of photoelectron spin from the molecular to the

laboratory frame, then projects it to the spin-detection axis $\hat{\mathbf{s}}^L$:

$$\hat{\mathbf{s}}^L \cdot \hat{\boldsymbol{\sigma}}_{\mu_1^M, \mu_2^M}^L = \hat{\mathbf{s}}^L \cdot \langle \chi_{\mu_1^M} | R_\rho \hat{\boldsymbol{\sigma}}^M | \chi_{\mu_2^M} \rangle = \hat{\mathbf{s}}^L \cdot R_\rho \langle \chi_{\mu_1^M} | \hat{\boldsymbol{\sigma}}^M | \chi_{\mu_2^M} \rangle = \hat{\mathbf{s}}^L \cdot \left(R_\rho \hat{\boldsymbol{\sigma}}_{\mu_1^M, \mu_2^M}^M \right). \quad (62)$$

Equation (60) can thus be written as

$$\begin{aligned} & \int d\rho W^M(\hat{\mathbf{k}}^M, \hat{\mathbf{s}}^L, \rho) \\ &= \frac{1}{2} \sum_{I, \mu_1^M, \mu_2^M} \int d\rho \left[\left(R_\rho \vec{\mathbf{D}}_{I, \vec{\mathbf{k}}^M, \mu_1^M}^{M*} \right) \cdot \vec{\mathbf{E}}^{L*} \right] \left[\left(R_\rho \vec{\mathbf{D}}_{I, \vec{\mathbf{k}}^M, \mu_2^M}^M \right) \cdot \vec{\mathbf{E}}^L \right] \left\{ \delta_{\mu_1^M, \mu_2^M} + \left[\hat{\mathbf{s}}^L \cdot \left(R_\rho \hat{\boldsymbol{\sigma}}_{\mu_1^M, \mu_2^M}^M \right) \right] \right\} \end{aligned} \quad (63)$$

The vectors that appear on the right-hand side of Eq. (63) can now be grouped into two sets:

(i) vectors that are fixed in the molecular frame such as the dipole transition vectors $\vec{\mathbf{D}}_{I, \vec{\mathbf{k}}^M, \mu^M}$, photoelectron momentum $\vec{\mathbf{k}}^M$, and photoelectron spin quantization axis $\hat{\boldsymbol{\sigma}}_{\mu_1^M, \mu_2^M}^M$, and (ii) vectors that are fixed in the laboratory frame such as spin detection axis $\hat{\mathbf{s}}^L$ and the electric field $\vec{\mathbf{E}}^L$. This will then allow us to use the technique in Ref. ⁵¹ in evaluating the orientation averaging $\int d\rho$ such that the resulting quantity can be expressed as $\sum_{ij} g_i M_{ij} f_j$, where, g_i and f_i are rotational invariants that are constructed from the two sets of vectors and M_{ij} is the coupling between the two rotational invariants. For our purposes, the following vector identities will be relevant:

$$\int d\rho (\vec{\mathbf{a}}^L \cdot \vec{\mathbf{u}}^L) \vec{\mathbf{b}}^L = \frac{1}{3} (\vec{\mathbf{a}}^M \cdot \vec{\mathbf{b}}^M) \vec{\mathbf{u}}^L \quad (64)$$

$$\int d\rho (\vec{\mathbf{a}}^L \cdot \vec{\mathbf{u}}^L) (\vec{\mathbf{b}}^L \cdot \vec{\mathbf{v}}^L) \vec{\mathbf{c}}^L = \frac{1}{6} [(\vec{\mathbf{a}}^M \times \vec{\mathbf{b}}^M) \cdot \vec{\mathbf{c}}^M] (\vec{\mathbf{u}}^L \times \vec{\mathbf{v}}^L) \quad (65)$$

$$\int d\rho (\vec{a}^L \cdot \vec{u}^L)(\vec{b}^L \cdot \vec{v}^L)(\vec{c}^L \cdot \vec{w}^L)\vec{d}^L = \frac{1}{30} \begin{bmatrix} (\vec{a}^M \cdot \vec{b}^M)(\vec{c}^M \cdot \vec{d}^M) \\ (\vec{a}^M \cdot \vec{c}^M)(\vec{b}^M \cdot \vec{d}^M) \\ (\vec{a}^M \cdot \vec{d}^M)(\vec{b}^M \cdot \vec{c}^M) \end{bmatrix}^T \begin{bmatrix} 4 & -1 & -1 \\ -1 & 4 & -1 \\ -1 & -1 & 4 \end{bmatrix} \begin{bmatrix} (\vec{u}^L \cdot \vec{v}^L)\vec{w}^L \\ (\vec{u}^L \cdot \vec{w}^L)\vec{v}^L \\ (\vec{v}^L \cdot \vec{w}^L)\vec{u}^L \end{bmatrix} \quad (66)$$

Spin-polarization The spin-resolved photoionization yield $W^L(\hat{s}^L)$ of a randomly oriented ensemble of molecules with the photoelectron spin measured along \hat{s}^L axis is

$$\begin{aligned} W^L(\hat{s}^L) &= \int d\Theta_k^L \int d\rho W^L(\hat{k}^L, \hat{s}^L, \rho) \\ &= \int d\rho \int d\Theta_k^L W^M(R_\rho^{-1}\hat{k}^L, R_\rho^{-1}\hat{s}^L, \rho) \\ &= \int d\Theta_k^M \int d\rho W^M(\hat{k}^M, \hat{s}^M, \rho), \end{aligned} \quad (67)$$

where, $\int d\Theta_k$ denotes integrating over all photoelectron ejection angles, while $W^L(\hat{k}^L, \hat{s}^L, \rho)$ and $W^M(\hat{k}^M, \hat{s}^M, \rho)$ are the spin and momentum-resolved yield for a given orientation ρ in the laboratory and molecular frame, respectively. The second line of Eq. (67) follows from the definition of a rotated function $W^L(\hat{k}^L, \hat{s}^L, \rho) = W^M(\hat{k}^M, \hat{s}^M, \rho)$ ⁵², and we have interchanged the order of integration to perform change of variable $\hat{k}^M = R_\rho^{-1}\hat{k}^L$ and again interchanged the order of integration since \hat{k}^M is now an integration variable independent of ρ .

Let us first evaluate the spin-resolved photoionization yield $W^L(\hat{s}^L)$, i.e.,

$$W^L(\hat{s}^L) = \int d\Theta_k^M \int d\rho W^M(\hat{k}^M, \hat{s}^L, \rho)$$

$$= \frac{1}{2} \sum_{I, \mu_1^M, \mu_2^M} \int d\Theta_k^M \int d\rho \left(\vec{\mathbf{D}}_{I, \vec{k}^M, \mu_1^M}^{L*} \cdot \vec{\mathbf{E}}^{L*} \right) \left(\vec{\mathbf{D}}_{I, \vec{k}^M, \mu_2^M}^L \cdot \vec{\mathbf{E}}^L \right) \left(\delta_{\mu_1^M, \mu_2^M} + \hat{\mathbf{s}}^L \cdot \hat{\boldsymbol{\sigma}}_{\mu_1^M, \mu_2^M}^L \right) \quad (68)$$

It follows from Eqs. (64) and (65) that

$$\int d\rho \left| \vec{\mathbf{D}}_{I, \vec{k}^M, \mu^M}^L \cdot \vec{\mathbf{E}}^L \right|^2 = \frac{1}{3} \left| \vec{\mathbf{D}}_{I, \vec{k}^M, \mu^M}^L \right|^2 \left| \vec{\mathbf{E}}^L \right|^2 \quad (69)$$

$$\begin{aligned} & \int d\rho \left(\vec{\mathbf{D}}_{I, \vec{k}^M, \mu_1^M}^{L*} \cdot \vec{\mathbf{E}}^{L*} \right) \left(\vec{\mathbf{D}}_{I, \vec{k}^M, \mu_2^M}^L \cdot \vec{\mathbf{E}}^L \right) \left(\hat{\mathbf{s}}^L \cdot \hat{\boldsymbol{\sigma}}_{\mu_1^M, \mu_2^M}^L \right) \\ &= \left[\hat{\boldsymbol{\sigma}}_{\mu_1^M, \mu_2^M}^M \cdot \left(i \vec{\mathbf{D}}_{I, \vec{k}^M, \mu_1^M}^{M*} \times \vec{\mathbf{D}}_{I, \vec{k}^M, \mu_2^M}^M \right) \right] \left[\hat{\mathbf{s}}^L \cdot \left(-i \vec{\mathbf{E}}^{L*} \times \vec{\mathbf{E}}^L \right) \right]. \end{aligned} \quad (70)$$

Equation (68) now evaluates to

$$W^L(\hat{\mathbf{s}}^L) = \frac{1}{6} \left\{ \sum_I \int d\Theta_k^M \left[\left| \vec{\mathbf{D}}_{I, \vec{k}^M, \frac{1}{2}}^M \right|^2 + \left| \vec{\mathbf{D}}_{I, \vec{k}^M, -\frac{1}{2}}^M \right|^2 \right] \right\} \left| \vec{\mathbf{E}}^L \right|^2 + \frac{1}{12} \left(\sum_{\mu_1, \mu_2} \hat{\boldsymbol{\sigma}}_{\mu_1, \mu_2}^M \cdot \vec{\Omega}_{\mu_1, \mu_2}^M \right) \left(\hat{\mathbf{s}}^L \cdot \vec{\Xi}^L \right) \quad (71)$$

where,

$$\vec{\Omega}_{\mu_1, \mu_2}^M = \sum_I \int d\Theta_k^M \left(i \vec{\mathbf{D}}_{I, \vec{k}^M, \mu_1^M}^{M*} \times \vec{\mathbf{D}}_{I, \vec{k}^M, \mu_2^M}^M \right) \quad (72)$$

is the spin-resolved curvature and $\vec{\Xi}^L = -i \vec{\mathbf{E}}^{L*} \times \vec{\mathbf{E}}^L = \xi |E_\omega^L|^2 \hat{\mathbf{z}}^L$ is the direction of photon spin.

It is straightforward to calculate the spin-polarization by taking the average of $\hat{\mathbf{s}}^L$, i.e.,

$$\langle \hat{\mathbf{s}}^L \rangle = \frac{\int d\Theta_s^L W^L(\hat{\mathbf{s}}^L) \hat{\mathbf{s}}^L}{\int d\Theta_s^L W^L(\hat{\mathbf{s}}^L)} = \frac{1}{3S_0} \left(\sum_{\mu_1, \mu_2} \hat{\boldsymbol{\sigma}}_{\mu_1, \mu_2}^M \cdot \vec{\Omega}_{\mu_1, \mu_2}^M \right) \hat{\Xi}^L = \frac{1}{3S_0} \text{Tr} \left(\hat{\Sigma}^M \cdot \Omega^M \right) \hat{\Xi}^L \quad (73)$$

$$S_0 = \left(\sum_{I, \mu^M} \int d\Theta_k^M \left| \vec{\mathbf{D}}_{I, \vec{k}^M, \mu^M}^M \right|^2 \right), \quad (74)$$

where the trace is performed over the spin coordinates and $\hat{\Sigma} = \hat{\boldsymbol{\sigma}}^T$.

Enantio-sensitive molecular orientation The orientation-averaged value of a vectorial observable \vec{V}^L of the molecular cation conditioned on the photoelectron spin detection axis \hat{s}^L is given by

$$\begin{aligned}\langle \vec{V}^L(\hat{s}^L) \rangle &= \int d\Theta_k^M \int d\rho W^M(\hat{k}^M, \hat{s}^M, \rho) \vec{V}^L \\ &= \frac{1}{2} \sum_{I, \mu_1^M, \mu_2^M} \int d\Theta_k^M \int d\rho \left(\vec{D}_{I, \vec{k}^M, \mu_1^M}^{L*} \cdot \vec{E}_p^{L*} \right) \left(\vec{D}_{I, \vec{k}^M, \mu_2^M}^L \cdot \vec{E}_p^L \right) \left(\delta_{\mu_1^M, \mu_2^M} + \hat{s}^L \cdot \hat{\sigma}_{\mu_1^M, \mu_2^M}^L \right) \vec{V}^L\end{aligned}\tag{75}$$

Let us first consider fields that are isotropically polarized in space. Suppose we have an arbitrary direction of linearly polarized field. Instead of a single direction that characterizes the direction of polarization, e.g., \hat{x}^L , we introduce

$$\vec{E}_p^L = E_\omega^L (\sin \theta_p \cos \varphi_p \hat{x}^L + \sin \theta_p \sin \varphi_p \hat{y}^L + \cos \theta_p \hat{z}^L)\tag{76}$$

Using Eq. (65), the first term of Eq. (75) simplifies into

$$\begin{aligned}\frac{1}{2} \sum_{I, \mu} \int d\Theta_k^M \int d\rho \left| \vec{D}_{\vec{k}^M, \mu^M}^L \cdot \vec{E}_p^L \right|^2 \vec{V}^L &= \frac{1}{12} \left[\left(\sum_{I, \mu} i \vec{D}_{\vec{k}^M, \mu^M}^{M*} \times \vec{D}_{\vec{k}^M, \mu^M}^M \right) \cdot \vec{V}^M \right] \left(-i \vec{E}_p^{L*} \times \vec{E}_p^L \right) \\ &= \frac{1}{12} \left[\left(\sum_{I, \mu} \vec{\Omega}_{I, \mu^M, \mu^M}^M \right) \cdot \vec{V}^M \right] \left(-i \vec{E}_p^{L*} \times \vec{E}_p^L \right)\end{aligned}\tag{77}$$

However, this term vanishes after averaging over all orientations of the field. Similarly, it follows from Eq. (66) that

$$\frac{1}{2} \sum_{I, \mu_1^M, \mu_2^M} \int d\Theta_k^M \int d\rho \left(\vec{D}_{I, \vec{k}^M, \mu_1^M}^{L*} \cdot \vec{E}_p^{L*} \right) \left(\vec{D}_{I, \vec{k}^M, \mu_2^M}^L \cdot \vec{E}_p^L \right) \left(\hat{s}^L \cdot \hat{\sigma}_{\mu_1^M, \mu_2^M}^L \right) \vec{V}^L$$

$$\begin{aligned}
&= \frac{1}{60} \sum_{I, \mu_1^M, \mu_2^M} \int d\Theta_k^M \begin{bmatrix} \left(\vec{\mathbf{D}}_{I, \vec{\mathbf{k}}^M, \mu_1^M}^{M*} \cdot \vec{\mathbf{D}}_{I, \vec{\mathbf{k}}^M, \mu_2^M}^M \right) \left(\hat{\boldsymbol{\sigma}}_{\mu_1^M, \mu_2^M}^M \cdot \vec{\mathbf{V}}^M \right) \\ \left(\vec{\mathbf{D}}_{I, \vec{\mathbf{k}}^M, \mu_1^M}^{M*} \cdot \hat{\boldsymbol{\sigma}}_{\mu_1^M, \mu_2^M}^M \right) \left(\vec{\mathbf{D}}_{I, \vec{\mathbf{k}}^M, \mu_2^M}^M \cdot \vec{\mathbf{V}}^M \right) \\ \left(\vec{\mathbf{D}}_{I, \vec{\mathbf{k}}^M, \mu_1^M}^{M*} \cdot \vec{\mathbf{V}}^M \right) \left(\vec{\mathbf{D}}_{I, \vec{\mathbf{k}}^M, \mu_2^M}^M \cdot \hat{\boldsymbol{\sigma}}_{\mu_1^M, \mu_2^M}^M \right) \end{bmatrix}^T \begin{bmatrix} 4 & -1 & -1 \\ -1 & 4 & -1 \\ -1 & -1 & 4 \end{bmatrix} \begin{bmatrix} |\vec{\mathbf{E}}_p^L|^2 \hat{\mathbf{s}}^L \\ (\vec{\mathbf{E}}_p^L \cdot \hat{\mathbf{s}}^L) \vec{\mathbf{E}}_p^L \\ (\vec{\mathbf{E}}_p^L \cdot \hat{\mathbf{s}}^L) \vec{\mathbf{E}}_p^{L*} \end{bmatrix} \\
\end{aligned} \tag{78}$$

in which, for brevity, we can rewrite as

$$\begin{aligned}
&\frac{1}{2} \sum_{I, \mu_1^M, \mu_2^M} \int d\Theta_k^M \int d\rho \left(\vec{\mathbf{D}}_{I, \vec{\mathbf{k}}^M, \mu_1^M}^{L*} \cdot \vec{\mathbf{E}}_p^{L*} \right) \left(\vec{\mathbf{D}}_{I, \vec{\mathbf{k}}^M, \mu_2^M}^L \cdot \vec{\mathbf{E}}_p^L \right) \left(\hat{\mathbf{s}}^L \cdot \hat{\boldsymbol{\sigma}}_{\mu_1^M, \mu_2^M}^L \right) \vec{\mathbf{V}}^L \\
&= \frac{1}{60} \begin{bmatrix} g_1 \\ g_2 \\ g_2^* \end{bmatrix}^T \begin{bmatrix} 4 & -1 & -1 \\ -1 & 4 & -1 \\ -1 & -1 & 4 \end{bmatrix} \begin{bmatrix} f_1 \\ f_2 \\ f_2^* \end{bmatrix} \\
&= \frac{1}{30} (2f_1 - \text{Re}[f_2]) g_1 - \frac{1}{30} (f_1 - 3\text{Re}[f_2]) \text{Re}[g_2] - \frac{1}{6} \text{Im}[f_2] \text{Im}[g_2]
\end{aligned} \tag{79}$$

Averaging over all orientations of the field, we then obtain

$$\begin{aligned}
&\frac{1}{2} \sum_{I, \mu_1^M, \mu_2^M} \int d\Theta_k^M \int d\rho \left(\vec{\mathbf{D}}_{I, \vec{\mathbf{k}}^M, \mu_1^M}^{L*} \cdot \vec{\mathbf{E}}_p^{L*} \right) \left(\vec{\mathbf{D}}_{I, \vec{\mathbf{k}}^M, \mu_2^M}^L \cdot \vec{\mathbf{E}}_p^L \right) \left(\hat{\mathbf{s}}^L \cdot \hat{\boldsymbol{\sigma}}_{\mu_1^M, \mu_2^M}^L \right) \vec{\mathbf{V}}^L \\
&= \frac{|E_\omega^L|^2}{18} \left\{ \left[\sum_{I, \mu_1^M, \mu_2^M} \int d\Theta_k^M \left(\vec{\mathbf{D}}_{I, \vec{\mathbf{k}}^M, \mu_1^M}^{M*} \cdot \vec{\mathbf{D}}_{I, \vec{\mathbf{k}}^M, \mu_2^M}^M \right) \hat{\boldsymbol{\sigma}}_{\mu_1^M, \mu_2^M}^M \right] \cdot \vec{\mathbf{V}}^M \right\} \hat{\mathbf{s}}^L
\end{aligned} \tag{80}$$

Thus,

$$\begin{aligned}
\langle \vec{\mathbf{V}}^L(\hat{\mathbf{s}}^L) \rangle_{\text{norm}}^{\text{unpol}} &= \frac{1}{3S_0} \left\{ \left[\sum_{I, \mu_1^M, \mu_2^M} \int d\Theta_k^M \left(\vec{\mathbf{D}}_{I, \vec{\mathbf{k}}^M, \mu_1^M}^{M*} \cdot \vec{\mathbf{D}}_{I, \vec{\mathbf{k}}^M, \mu_2^M}^M \right) \hat{\boldsymbol{\sigma}}_{\mu_1^M, \mu_2^M}^M \right] \cdot \vec{\mathbf{V}}^M \right\} \hat{\mathbf{s}}^L \\
&= \frac{1}{3S_0} (\vec{\mathbf{S}}^M \cdot \vec{\mathbf{V}}^M) \hat{\mathbf{s}}^L
\end{aligned} \tag{81}$$

where, we have normalized by the total yield

$$\int d\Theta_s^L \int d\Theta_k^M \int d\rho W^M(\hat{\mathbf{k}}^M \hat{\mathbf{s}}^M, \rho) = \frac{1}{6} S_0 \quad (82)$$

A similar straightforward calculation for circularly polarized light will yield

$$\langle \vec{\mathbf{V}}^L(\hat{\mathbf{s}}^L) \rangle_{\text{norm}}^{\text{circ}} = \langle \vec{\mathbf{V}}^L(\hat{\mathbf{s}}^L) \rangle_S + \langle \vec{\mathbf{V}}^L(\hat{\mathbf{s}}^L) \rangle_\Omega \quad (83)$$

$$\begin{aligned} \langle \vec{\mathbf{V}}^L(\hat{\mathbf{s}}^L) \rangle_\Omega &= \frac{1}{2S_0} \left\{ \left[\sum_{I,\mu^M} \int d\Theta_k^M \left(i \vec{\mathbf{D}}_{I,\vec{\mathbf{k}}^M, \mu^M}^{M*} \times \vec{\mathbf{D}}_{I,\vec{\mathbf{k}}^M, \mu^M}^M \right) \right] \cdot \hat{\mathbf{V}}^M \right\} \hat{\mathbf{\Xi}}^L \\ &\quad + \frac{1}{2S_0} \left\{ \left[\sum_{I,\mu_1^M, \mu_2^M} \hat{\boldsymbol{\sigma}}_{\mu_1^M, \mu_2^M}^M \times \int d\Theta_k^M \left(i \vec{\mathbf{D}}_{I,\vec{\mathbf{k}}^M, \mu_1^M}^{M*} \times \vec{\mathbf{D}}_{I,\vec{\mathbf{k}}^M, \mu_2^M}^M \right) \right] \cdot \hat{\mathbf{V}}^M \right\} (\hat{\mathbf{s}}^L \times \hat{\mathbf{\Xi}}^L) \\ &= \frac{1}{2S_0} (\text{Tr}(\boldsymbol{\Omega}^M) \cdot \hat{\mathbf{V}}^M) + \frac{1}{2S_0} \left\{ [\text{Tr}(\hat{\boldsymbol{\Sigma}}^M \times \boldsymbol{\Omega}^M)] \cdot \hat{\mathbf{V}}^M \right\} (\hat{\mathbf{s}}^L \times \hat{\mathbf{\Xi}}^L) \end{aligned} \quad (84)$$

$$\begin{aligned} \langle \vec{\mathbf{V}}^L(\hat{\mathbf{s}}^L) \rangle_S &= \frac{1}{10S_0} \left\{ \left[\sum_{I,\mu_1^M, \mu_2^M} \int d\Theta_k^M \left(\vec{\mathbf{D}}_{I,\vec{\mathbf{k}}^M, \mu_1^M}^{M*} \cdot \vec{\mathbf{D}}_{I,\vec{\mathbf{k}}^M, \mu_2^M}^M \right) \hat{\boldsymbol{\sigma}}_{\mu_1^M, \mu_2^M}^M \right] \cdot \hat{\mathbf{V}}^M \right\} [3\hat{\mathbf{s}}^L + (\hat{\mathbf{s}}^L \cdot \hat{\mathbf{z}}^L) \hat{\mathbf{z}}^L] \\ &\quad + \frac{1}{10S_0} \left\{ \text{Re} \left[\sum_{I,\mu_1^M, \mu_2^M} \int d\Theta_k^M \left(\vec{\mathbf{D}}_{I,\vec{\mathbf{k}}^M, \mu_1^M}^{M*} \cdot \hat{\boldsymbol{\sigma}}_{\mu_1^M, \mu_2^M}^M \right) \vec{\mathbf{D}}_{I,\vec{\mathbf{k}}^M, \mu_2^M}^M \right] \cdot \hat{\mathbf{V}}^M \right\} [\hat{\mathbf{s}}^L - 3(\hat{\mathbf{s}}^L \cdot \hat{\mathbf{z}}^L) \hat{\mathbf{z}}^L] \\ &= \frac{1}{10S_0} (\vec{\mathbf{S}}^M \cdot \hat{\mathbf{V}}^M) [3\hat{\mathbf{s}}^L + (\hat{\mathbf{s}}^L \cdot \hat{\mathbf{z}}^L) \hat{\mathbf{z}}^L] + \frac{1}{10S_0} (\vec{\mathbf{S}}'^M \cdot \hat{\mathbf{V}}^M) [\hat{\mathbf{s}}^L - 3(\hat{\mathbf{s}}^L \cdot \hat{\mathbf{z}}^L) \hat{\mathbf{z}}^L] \end{aligned} \quad (85)$$

E Estimating the degree of orientation

An estimate of the number of ‘head’ $N_{+\hat{x}_i}$ and ‘tail’ $N_{-\hat{x}_i}$ molecules corresponding to averaged angle $\langle \hat{\mathbf{e}}^L \cdot \hat{x}_i^L \rangle$ between the vector $\hat{\mathbf{e}}^L$ and “target” orientation axis \hat{x}_i^L , can be performed by

adopting the methods of Ref. ³¹ to model the angular distribution of oriented molecules. Let

$$\Psi(\theta, \varphi) = a_0 Y_{0,0}(\theta, \varphi) + b_0 Y_{1,0}(\theta, \varphi) + \frac{b_-}{\sqrt{2}} [Y_{1,-1}(\theta, \varphi) - Y_{1,1}(\theta, \varphi)] + i \frac{b_+}{\sqrt{2}} [Y_{1,-1}(\theta, \varphi) + Y_{1,1}(\theta, \varphi)], \quad (86)$$

where $|a_0|^2 + |b_0|^2 + |b_-|^2 + |b_+|^2 = 1$. Hence,

$$\begin{aligned} \langle \hat{\mathbf{e}}^L \cdot \hat{\mathbf{x}}^L \rangle &= \int d\Omega \sin \theta \cos \varphi |\Psi(\Omega)|^2 = \frac{2}{\sqrt{3}} \operatorname{Re}[a_0 b_-^*] \\ \langle \hat{\mathbf{e}}^L \cdot \hat{\mathbf{y}}^L \rangle &= \int d\Omega \sin \theta \sin \varphi |\Psi(\Omega)|^2 = \frac{2}{\sqrt{3}} \operatorname{Re}[a_0 b_+^*] \\ \langle \hat{\mathbf{e}}^L \cdot \hat{\mathbf{z}}^L \rangle &= \int d\Omega \cos \theta |\Psi(\Omega)|^2 = \frac{2}{\sqrt{3}} \operatorname{Re}[a_0 b_0^*] = \frac{1}{2} \left(1 + \frac{3}{2} \right) \end{aligned} \quad (87)$$

As an example, let us consider the number of ‘head’ molecules $N_{+\hat{\mathbf{z}}}$ oriented along $\hat{\mathbf{z}}^L$, i.e.,

$$N_{+\hat{\mathbf{z}}} = \int_0^{2\pi} d\varphi \int_0^{\pi/2} d\theta \sin \theta |\Psi(\theta, \varphi)|^2 \cos \theta = \frac{1}{2} \left(1 + \frac{3}{2} \langle \hat{\mathbf{e}}^L \cdot \hat{\mathbf{z}}^L \rangle \right) \quad (88)$$

$$N_{-\hat{\mathbf{z}}} = 1 - N_{+\hat{\mathbf{z}}}. \quad (89)$$

F Spin-polarization of synthetic chiral Argon states

Spin-polarization (i.e. χ_{gs}) in photoionization from chiral states of Ar $|\psi_{m,\mu}^\pm\rangle$ by circularly polarised light with $\varsigma = +1$ as a function of the photoelectron momentum is shown in Figure 10. Note that (i) maximum spin polarization can reach $2\chi_{gs} \simeq 14\%$, and (ii) the depolarization of the initial spin orientation is highly sensitive to the initial state. In particular, comparing violet and orange curves (Fig. 10(a)) for $k = 0.4 - 1.5$ a.u. shows the spin-up state depolarizes by almost 90%, whereas the spin-down state repolarizes by 114%. Black curves show spin-polarization of initially co- (Fig. 10(a)) and counter-rotating (Fig. 10(a)) electrons from states with depolarised spin.

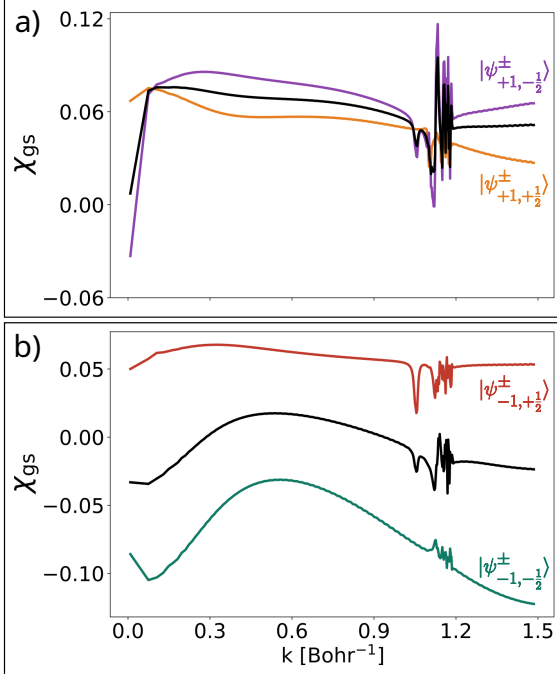


Figure 10: Geometric spin susceptibility χ_{gs} quantifying spin polarization for the chiral superpositions $|\psi_{m,\mu}^\pm\rangle$ along the direction of photon spin $\hat{\Xi}^L$. (a) $m = 1$, $\mu = \pm \frac{1}{2}$ (violet and yellow correspondingly) and averaged over spin orientation in initial state (black), (b) The same for $m = -1$, $\mu = \pm \frac{1}{2}$ (red and green correspondingly) and averaged black. The rapidly oscillating behavior at higher values of k are due to the Fano resonances, leading up to the ionization threshold for the 3s electrons ^{37,53}.

Thus, spin polarization of molecular targets by circularly polarised fields has geometric origin and emerges due to preferential ionization of species in which the curvature is oriented parallel to the photon spin.

1. Evers, F. *et al.* Theory of chirality induced spin selectivity: Progress and challenges. *Advanced Materials* **34**, 2106629 (2022).

2. Aiello, C. D. *et al.* A chirality-based quantum leap. *ACS nano* **16**, 4989–5035 (2022).
3. Gaita-Ariño, A., Luis, F., Hill, S. & Coronado, E. Molecular spins for quantum computation. *Nature chemistry* **11**, 301–309 (2019).
4. Atzori, M. & Sessoli, R. The second quantum revolution: role and challenges of molecular chemistry. *Journal of the American Chemical Society* **141**, 11339–11352 (2019).
5. Wasielewski, M. R. *et al.* Exploiting chemistry and molecular systems for quantum information science. *Nature Reviews Chemistry* **4**, 490–504 (2020).
6. Carretta, S., Zueco, D., Chiesa, A., Gómez-León, Á. & Luis, F. A perspective on scaling up quantum computation with molecular spins. *Applied Physics Letters* **118** (2021).
7. Heinrich, A. J. *et al.* Quantum-coherent nanoscience. *Nature nanotechnology* **16**, 1318–1329 (2021).
8. Chiesa, A. *et al.* Chirality-induced spin selectivity: An enabling technology for quantum applications. *Advanced Materials* **35**, 2300472 (2023).
9. Ray, K., Ananthavel, S., Waldeck, D. & Naaman, R. Asymmetric scattering of polarized electrons by organized organic films of chiral molecules. *Science* **283**, 814–816 (1999).
10. Ray, S., Daube, S., Leitus, G., Vager, Z. & Naaman, R. Chirality-induced spin-selective properties of self-assembled monolayers of dna on gold. *Physical review letters* **96**, 036101 (2006).

11. Kettner, M. *et al.* Chirality-dependent electron spin filtering by molecular monolayers of helicenes. *The journal of physical chemistry letters* **9**, 2025–2030 (2018).
12. Mishra, D. *et al.* Spin-dependent electron transmission through bacteriorhodopsin embedded in purple membrane. *Proceedings of the National Academy of Sciences* **110**, 14872–14876 (2013).
13. Kettner, M., Bhowmick, D. K., Bartsch, M., Göhler, B. & Zacharias, H. A silicon-based room temperature spin source without magnetic layers. *Advanced Materials Interfaces* **3** (2016).
14. Yeganeh, S., Ratner, M. A., Medina, E. & Mujica, V. Chiral electron transport: Scattering through helical potentials. *The Journal of chemical physics* **131** (2009).
15. Medina, E., López, F., Ratner, M. A. & Mujica, V. Chiral molecular films as electron polarizers and polarization modulators. *Europhysics Letters* **99**, 17006 (2012).
16. Eremko, A. & Loktev, V. Spin sensitive electron transmission through helical potentials. *Physical Review B—Condensed Matter and Materials Physics* **88**, 165409 (2013).
17. Varela, S., Medina, E., Lopez, F. & Mujica, V. Inelastic electron scattering from a helical potential: transverse polarization and the structure factor in the single scattering approximation. *Journal of Physics: Condensed Matter* **26**, 015008 (2013).
18. Gutierrez, R., Díaz, E., Naaman, R. & Cuniberti, G. Spin-selective transport through helical molecular systems. *Physical Review B—Condensed Matter and Materials Physics* **85**, 081404 (2012).

19. Guo, A.-M. & Sun, Q.-f. Spin-selective transport of electrons in dna double helix. *Physical review letters* **108**, 218102 (2012).
20. Matityahu, S., Utsumi, Y., Aharony, A., Entin-Wohlman, O. & Balseiro, C. A. Spin-dependent transport through a chiral molecule in the presence of spin-orbit interaction and nonunitary effects. *Physical Review B* **93**, 075407 (2016).
21. Varela, S., Mujica, V. & Medina, E. Effective spin-orbit couplings in an analytical tight-binding model of dna: Spin filtering and chiral spin transport. *Physical Review B* **93**, 155436 (2016).
22. Peter, J. S., Ostermann, S. & Yelin, S. F. Chirality dependent photon transport and helical superradiance. *Phys. Rev. Res.* **6**, 023200 (2024). URL <https://link.aps.org/doi/10.1103/PhysRevResearch.6.023200>.
23. Maslyuk, V. V., Gutierrez, R., Dianat, A., Mujica, V. & Cuniberti, G. Enhanced magnetoresistance in chiral molecular junctions. *The journal of physical chemistry letters* **9**, 5453–5459 (2018).
24. Díaz, E., Domínguez-Adame, F., Gutierrez, R., Cuniberti, G. & Mujica, V. Thermal decoherence and disorder effects on chiral-induced spin selectivity. *The journal of physical chemistry letters* **9**, 5753–5758 (2018).
25. Zoöllner, M. S., Varela, S., Medina, E., Mujica, V. & Herrmann, C. Insight into the origin of chiral-induced spin selectivity from a symmetry analysis of electronic transmission. *Journal of chemical theory and computation* **16**, 2914–2929 (2020).

26. Ghazaryan, A., Lemeshko, M. & Volosniev, A. G. Filtering spins by scattering from a lattice of point magnets. *Communications Physics* **3**, 178 (2020).
27. Fransson, J. Chirality-induced spin selectivity: The role of electron correlations. *The journal of physical chemistry letters* **10**, 7126–7132 (2019).
28. Shitade, A. & Minamitani, E. Geometric spin–orbit coupling and chirality-induced spin selectivity. *New Journal of Physics* **22**, 113023 (2020).
29. Varela, S., Gutierrez, R., Cuniberti, G., Medina, E. & Mujica, V. Chiral spin selectivity and chiroptical activity in helical molecules. *The Journal of Chemical Physics* **161** (2024).
30. Ordonez, A. F. & Smirnova, O. Propensity rules in photoelectron circular dichroism in chiral molecules. I. Chiral hydrogen. *Physical Review A* **99**, 043416 (2019). URL <https://link.aps.org/doi/10.1103/PhysRevA.99.043416>.
31. Ordonez, A. F., Ayuso, D., Decleva, P. & Smirnova, O. Geometric magnetism and anomalous enantio-sensitive observables in photoionization of chiral molecules. *Communications Physics* **6**, 257 (2023).
32. Ordonez, A. F., Roos, A., Maier, P. M., Ayuso, D. & Smirnova, O. Geometry of temporal chiral structures. *arXiv preprint arXiv:2409.02500* (2024).
33. Roos, A., Maier, P. M., Ordonez, A. F. & Smirnova, O. Geometry of chiral temporal structures ii: The formalism. *arXiv preprint arXiv:2505.22744* (2025).

34. Ordonez, A. F. & Smirnova, O. Propensity rules in photoelectron circular dichroism in chiral molecules. i. chiral hydrogen. *Physical Review A* **99**, 043416 (2019).
35. Carlström, S., Spanner, M. & Patchkovskii, S. General time-dependent configuration-interaction singles. i. molecular case. *Physical Review A* **106**, 043104 (2022).
36. Carlström, S., Bertolino, M., Dahlström, J. M. & Patchkovskii, S. General time-dependent configuration-interaction singles. ii. atomic case. *Physical Review A* **106**, 042806 (2022).
37. Carlström, S. *et al.* Spin-polarized photoelectrons in the vicinity of spectral features. *Physical Review Letters* **134**, 093202 (2025).
38. Suzuki, Y.-I. Communication: Photoionization of degenerate orbitals for randomly oriented molecules: The effect of time-reversal symmetry on recoil-ion momentum angular distributions. *The Journal of chemical physics* **148** (2018).
39. Wanie, V. *et al.* Capturing electron-driven chiral dynamics in uv-excited molecules. *Nature* 1–7 (2024).
40. Cherepkov, N. Theory of spin polarisation phenomena in molecular photoionisation processes. *Journal of Physics B: Atomic and Molecular Physics* **14**, 2165 (1981).
41. Cherepkov, N. Manifestations of the optical activity of molecules in the dipole photoeffect. *Journal of Physics B: Atomic and Molecular Physics* **16**, 1543 (1983).

42. Flores, P. C. M., Carlström, S., Patchkovskii, S., Ordonez, A. F. & Smirnova, O. Enantio-sensitive spin polarization vortices in one-photon ionization by circularly polarized light. *In preparation* (2024).
43. Flores, P. C. M., Carlström, S., Patchkovskii, S., Ordonez, A. F. & Smirnova, O. Geometric magnetism links chirality and spin in photoionization by circularly polarized fields. *In preparation* (2024).
44. Artemyev, A. *et al.* Photoelectron circular dichroism in the spin-polarized spectra of chiral molecules. *Physical Review Letters* **132**, 123202 (2024).
45. Heinzmann, U. Experimental determination of the phase differences of continuum wavefunctions describing the photoionisation process of xenon atoms. ii. evaluation of the matrix elements and the phase differences and their comparison with data in the discrete spectral range in application of the multichannel quantum defect theory. *Journal of Physics B: Atomic and Molecular Physics* **13**, 4367 (1980).
46. Nicklass, A., Dolg, M., Stoll, H. & Preuss, H. *Ab Initio* energy-adjusted pseudopotentials for the noble gases Ne through Xe: Calculation of atomic dipole and quadrupole polarizabilities. *The Journal of Chemical Physics* **102**, 8942–8952 (1995). URL <https://doi.org/10.1063/1.468948>.
47. Pabst, S., Lein, M. & Wörner, H. J. Preparing attosecond coherences by strong-field ionization. *Physical Review A* **93**, 023412 (2016). URL <http://dx.doi.org/10.1103/PhysRevA.93.023412>.

48. Zapata, F., Vinbladh, J., Ljungdahl, A., Lindroth, E. & Dahlström, J. M. Relativistic time-dependent configuration-interaction singles method. *Physical Review A* **105**, 012802 (2022). URL <http://dx.doi.org/10.1103/PhysRevA.105.012802>.
49. Ruberti, M., Averbukh, V. & Mintert, F. Bell test of quantum entanglement in attosecond photoionization. *Physical Review X* **14**, 041042 (2024). URL <http://dx.doi.org/10.1103/PhysRevX.14.041042>.
50. Mogensen, P. K. & Riseth, A. N. Optim: A mathematical optimization package for Julia. *Journal of Open Source Software* **3**, 615 (2018).
51. Andrews, D. L. & Thirunamachandran, T. On three-dimensional rotational averages. *The Journal of Chemical Physics* **67**, 5026–5033 (1977).
52. Brink, D. & Sactchler, G. Angular momentum, claren (1968).
53. Samson, J. & Stolte, W. Precision measurements of the total photoionization cross-sections of He, Ne, Ar, Kr, and Xe. *Journal of Electron Spectroscopy and Related Phenomena* **123**, 265–276 (2002). URL [http://dx.doi.org/10.1016/S0368-2048\(02\)00026-9](http://dx.doi.org/10.1016/S0368-2048(02)00026-9).